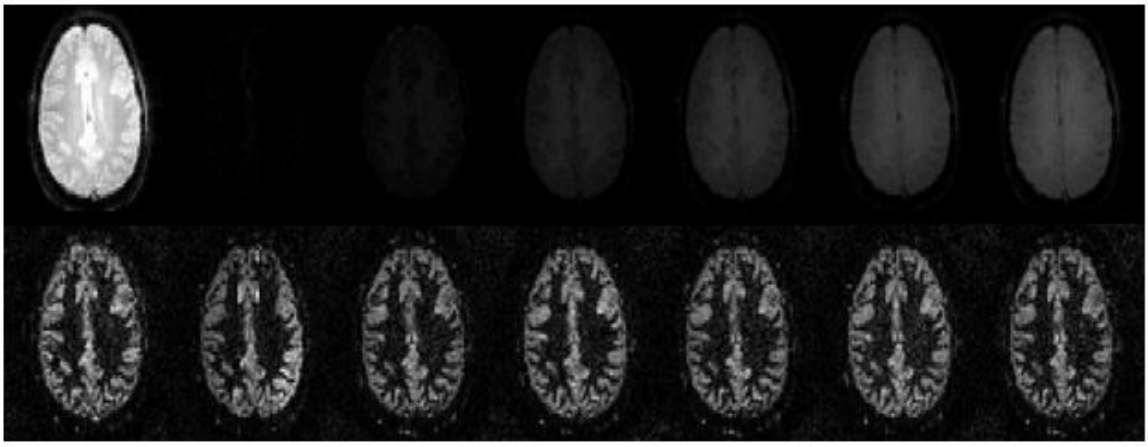

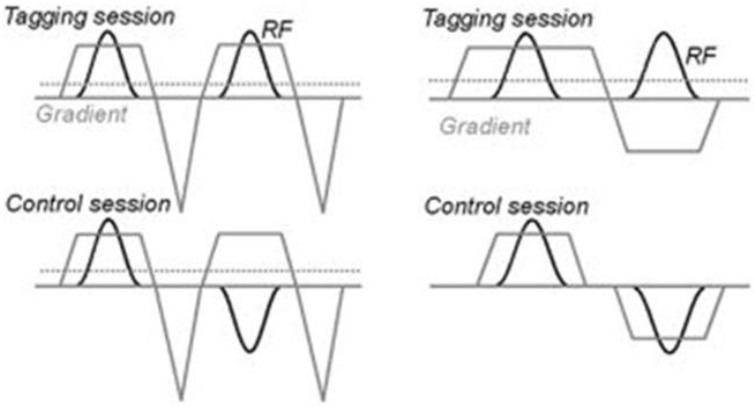

Cátia Filipa Mota Nunes

Sequence Optimization in Pseudo-Continuous Arterial Spin Labeling

Dissertação de Mestrado em Engenharia Biomédica no ramo de Neurociências
apresentada no Departamento de Física da Universidade de Coimbra

Fevereiro de 2015

· U C ·

UNIVERSIDADE DE COIMBRA

• U C •
FCTUC FACULDADE DE CIÊNCIAS
E TECNOLOGIA
UNIVERSIDADE DE COIMBRA

Cátia Filipa Mota Nunes

Sequence Optimization in Pseudo-Continuous Arterial Spin Labeling

Dissertation presented to the Faculty of Sciences and Technology of the University of Coimbra to fulfill the requirements to obtain a Master's degree in Biomedical Engineering

Supervisors:
Rolf Pohmann (PhD)
Miguel Castelo Branco (M.D., PhD)

Coimbra, 2015

This thesis was developed in collaboration with:

Max Planck Institute for Biological Cybernetics, Magnetic Resonance Center, Tübingen, Germany

Esta cópia da tese é fornecida na condição de que quem a consulta reconhece que os direitos de autor são pertença do autor da tese e que nenhuma citação ou informação obtida a partir dela pode ser publicada sem a referência apropriada.

This copy of the thesis has been supplied on condition that anyone who consults it is understood to recognize that its copyright rests with its author and that no quotation from the thesis and no information derived from it may be published without proper acknowledgement.

Acknowledgments

First of all, I would like to thank Dr. Rolf Pohmann for his enduring patience, availability and intellectual contribution to this thesis. Though busy with several other studies, Dr. Rolf always found the time for guidance and discussion. I am also deeply grateful for the understanding, support and knowledge shared during the development of the project.

In addition, I thank Prof. Dr. Klaus Scheffler for granting me the opportunity of developing my master thesis at the Max Planck Institute for Biological Cybernetics. Also, I am grateful for all the assistance in finding a group and project that matches my interests and for providing the necessary work conditions to the fulfillment of this dissertation. Furthermore, I want to leave a word of appreciation to Prof. Dr. Miguel Castelo Branco for his interest, mentorship and cooperation. I am thankful for the advice regarding the choice of the project/institution and also for the support and opportunities offered to the students of Biomedical Engineering.

My thanks to other students, researchers and staff for all the help provided during my stay. In particular, I would like to thank Joana for introducing me to SPM, Sahar and Paul for the professional advice and support, and Hildegard for the interest and care. I would also like to give a special thanks to Carolina for all the patience and enthusiasm. I could not wish for a more helpful and supportive office mate and friend. My thanks extend to Lucy and Jelly for the friendship, support, encouragement and also for taking part in the experimental studies.

Finally, I would like to thank my family and boyfriend for all the affection and care. This thesis is the result of their constant encouragement and unwavering support.

Abstract

Arterial spin labeling (ASL) is a Magnetic Resonance (MR) technique that provides quantitative measures of regional Cerebral Blood Flow (CBF), non-invasively, using arterial blood water as an endogenous tracer. Abnormalities or disruption in the perfusion process can have major effects, especially in the brain which is a highly perfused organ. In fact, several pathological conditions (including acute stroke, brain tumors, neurodegenerative diseases and epilepsy) are associated with abnormal CBF values. Therefore, ASL has a critical value in the diagnosis and monitoring of treatment for brain diseases.

Pseudo-continuous ASL (pCASL) is the recommended implementation method for ASL studies since it combines the advantages of previous methods, a high signal-to-noise ratio (SNR) and inversion efficiency. The aim of this work is the optimization and implementation of a pCASL sequence developed in-house.

A total of four studies were carried out to evaluate the performance of the sequence parameters for measuring gray matter perfusion and the impact in image quality of two different head coils: i) determination of the optimal bandwidth and flip angle of the inversion pulses, ii) implementation of full and incomplete background suppression, iii) comparison of balanced and unbalanced pCASL and readout sequences namely Echo Planar Imaging (EPI) and True Fast Imaging with Steady-state free Precession (TrueFISP) and iv) comparison of the quality of perfusion images obtained with two different head coils. Perfusion images were acquired through experimental measurements in healthy volunteers for each study conducted. Data analysis was performed with homemade MATLAB and SPM8 software and the impact of the different parameters on the SNR and on the resulting CBF values was evaluated.

Considering the parameters tested, the results analysis suggests the use of a Gaussian inversion pulse, flip angle equal to 24º or 28º and full background suppression, in order to maximize the SNR of the resulting images. The outcome is in accordance with previous findings concerning the influence of background suppression and flip angle in the SNR. The major contribution of the current work consisted in the development of a reliable sequence well suited for future experimental investigations of cerebral perfusion. Future

work consists in testing the ability of the sequence to detect perfusion changes in functional studies.

Keywords: Magnetic Resonance Imaging; Arterial Spin Labeling; Pseudo-Continuous Arterial Spin Labeling; Experimental Optimization; Sequence.

Resumo

Arterial Spin Labeling (ASL) é uma técnica de Ressonância Magnética que fornece medidas quantitativas de fluxo sanguíneo cerebral (FSC) regional, de forma não invasiva, utilizando a água presente no sangue arterial como um marcador endógeno. Anormalidades ou perturbações no processo de perfusão podem ter efeitos marcantes, especialmente no cérebro, que é um órgão muito perfundido. De facto, várias condições patológicas (nomeadamente acidentes vasculares cerebrais agudos, tumores cerebrais, doenças neurodegenerativas e epilepsia) estão associadas a valores anormais de FSC. Portanto, ASL tem um valor fundamental no diagnóstico e acompanhamento do tratamento de doenças do cérebro.

Pseudo-continuous ASL (pCASL) é o método de implementação recomendado para estudos ASL, uma vez que combina as vantagens de métodos anteriores, uma elevada relação sinal-ruído (S/N) e eficiência de inversão. O objetivo deste trabalho consiste na otimização e implementação de uma sequência pCASL desenvolvida *in-house*.

Foram realizados quatro estudos para avaliar o desempenho dos parâmetros da sequência para medir perfusão na matéria cinzenta e o impacto na qualidade da imagem usando dois *head coils* diferentes: i) determinação da largura de banda e *flip angle* ótimos dos pulsos de inversão, ii) implementação de supressão do sinal do tecido estático completa e incompleta, iii) comparação de *balanced*/ *unbalanced* pCASL e sequências de aquisição nomeadamente *Echo Planar Imging* (EPI) e True Fast Imaging with Steady-state free Precession (TrueFISP) e iv) comparação da qualidade das imagens de perfusão obtidas com dois *head coils* diferentes. As imagens de perfusão foram adquiridas através de medições experimentais em voluntários saudáveis, para cada estudo. A análise dos dados foi realizada com o *software* MATLAB, usando *scripts* programados *in-house* e SPM8, e o impacto dos diferentes parâmetros no S/N e no FSC resultantes foi avaliado.

Considerando os parâmetros testados, a análise dos resultados sugere o uso de pulsos de inversão Gauss, *flip angle* igual a 24º ou 28º e supressão completa do sinal estático, a fim de maximizar o S/N das imagens resultantes. Os resultados estão de acordo com publicações anteriores sobre a influência da supressão do sinal do tecido estático e *flip angle* no S/N. A maior contribuição deste trabalho consistiu no desenvolvimento de uma sequência de confiança adequada para futuras investigações experimentais de perfusão

cerebral. No futuro seria interessante testar a capacidade da sequência para detetar alterações de perfusão em estudos funcionais.

Palavras-Chave: Ressonância Magnética; *Arterial Spin Labeling; Pseudo-Continuous Arterial Spin Labeling*; Otimização Experimental; Sequência.

Symbols

$\boldsymbol{\alpha}$ – Inversion efficiency

$\boldsymbol{\gamma}$ – Gyromagnetic ratio

$\boldsymbol{\lambda}$ – Blood/brain coefficient of water

$\boldsymbol{\omega}$ – Larmor frequency

$\Delta\mathbf{M}$ – Perfusion weighted image

$\Delta\mathbf{t}$ – Post labeling delay

$\boldsymbol{B_0}$ – Static Magnetic field

$\boldsymbol{f}$ – Cerebral Blood Flow

$\mathbf{G_{x,y,z}}$ – Gradient in the x, y or z direction

M – Net magnetization of all spins within a spin system

$\mathbf{M_{x,y,z}}$ – Net Magnetization of all spins within a spin system in x, y, or z direction

$\boldsymbol{M_0}$ – Reference scan

$\mathbf{T_1}$ – The time constant that describes the recovery of the longitudinal component of magnetization over time

$\boldsymbol{T_{1g}}$ – Gray matter T_1

$\mathbf{T_2}$ – The time constant that describes the decay of the transverse component of net magnetization over time

$\mathbf{T_2^*}$ – The time constant that describes the loss of signal strength due to static field non-uniformity and spin-spin interactions

$^{\mathbf{15}}\mathbf{O}$ – Radionuclide Oxygen-15

Abbreviations

2D – Two Dimensions

3D – Three Dimensions

AC-PC – Anterior Comissure-Posterior Commissure

AFP – Adiabatic Fast Passage

ANOVA – Analysis of Variance

ASL – Arterial Spin Labeling

ATT – Arterial Transit Time

a.u. – Arbitrary units

BG – Background Suppression

bSSFP – Balanced Steady-State Free Precession

CASL – Continuous Arterial Spin Labeling

CBF – Cerebral Blood Flow

CSF – Cerebrospinal Fluid

DSC MRI – Dynamic Susceptibility Contrast Magnetic Resonance Imaging

EPI – Echo Planar Imaging

FA – Flip Angle

FAIR – Flow Sensitive Alternating Inversion Recovery

fMRI – Functional Magnetic Resonance Imaging

FOV – Field Of View

FT – Fourier Transform

GE – Gradient Echo

GM – Gray Matter

GRASE – Gradient Echo and Spin Echo

GREASE – Gradient Echo Asymmetric Spin Echo

ICA – Internal Carotid Artery

MPRAGE – Magnetization Prepared Rapid Gradient Echo

MR – Magnetic Resonance

MRI – Magnetic Resonance Imaging

MT – Magnetization Transfer

NMR – Nuclear Magnetic Resonance

PASL – Pulsed Arterial Spin Labeling

pCASL – pseudo-Continuous Arterial Spin Labeling

PET – Positron Emission Tomography

RARE – Rapid Acquisition with Refocused Echoes

RF – Radio Frequency

SAR – Specific Absorption Rate

SD – Standard Deviation

SE – Spin Echo

SNR – Signal to Noise Ratio

SPM – Statistical Parametric Mapping

SSFP – Steady-State Free Precession

sSNR – Spatial Signal to Noise Ratio

STAR – Signal Targeting with Alternating Radiofrequency

TE – Echo Time

TR – Repetition Time

TrueFISP – True Fast Imaging with Steady-state Precession

tSNR –Temporal Signal to Noise Ratio

VA – Vertebral Artery

WM – White Matter

Figures Index

Tables Index

Contents

Chapter 1

Introduction

1.1 Motivation and Objectives

Arterial Spin Labeling (ASL) is a Magnetic Resonance (MR) modality whose purpose is the measurement of perfusion, that is, the delivery of oxygen and nutrients to tissues by means of blood flow [1]. This nutritive supply is fundamental to maintain healthy tissue and is a main indicator of viability and function. Perfusion can also be referred to as Cerebral Blood Flow (CBF) and is measured in units of millimeter of blood per gram of tissue per unit of time (ml/g/min) [2].

The concept of ASL for perfusion imaging was conceived in the 90's [3-5]. In brief, ASL techniques use endogenous arterial blood water as a tracer similar to positron emission tomography (PET) CBF measurements, which use ^{15}O labeled water as the flow tracer. The arterial blood water is magnetically "labeled" using radiofrequency (RF) irradiation. The labeling is followed by a waiting period to allow the blood to flow from the tagged location to the imaged area. This process is then repeated without the labeling to acquire a control image. The perfusion image is obtained by the difference between tag and control images [1, 5]. Since the signal of the magnetic labeled water decays with T_1 in the order of few seconds, the use of a fast readout sequence is essential [1].

While the focus of initial ASL studies was technological development and validation, since then several robust ASL implementations have emerged, and ASL is currently available on multiple platforms. Consequently, the applications of ASL have begun to grow, not only in basic research but also clinically, in part due to its non-invasive nature and ability to quantitatively measure tissue perfusion [6]. These benefits make ASL very suitable for perfusion studies in healthy individuals, patients with renal insufficiency and those who need repetitive follow-ups [7]. Even though ASL can be carried out in any organ, most studies to date have focused on the brain. With the maturation of the technique it became possible to obtain whole-brain ASL data routinely in both clinical and research settings [7, 8].

Perfusion provides oxygen and nutrients to tissues and is closely tied to tissue function. Disorders of perfusion such as stroke are a major source of medical morbidity and mortality. Furthermore, blood flow alterations also commonly accompany other pathophysiological changes, such as cancer, epilepsy, and neurodegenerative diseases [9]. ASL is particularly suited for clinical neurosciences, given that it can provide a characterization of cerebrovascular diseases with a primary disturbance of CBF. Moreover, neurodegenerative disorders can also be studied and evaluated with this technique, since in the early stages of diseases such as Alzheimer and dementia, the patients exhibit perturbations in CBF [1, 7]. Up until now, ASL has been used clinically for disease detection, disease induced damage assessment, treatment monitoring and therapy evaluation [10].

Even though many technical improvements have been done in the past years, ASL continues to suffer from low signal-to-noise ratio (SNR), hence the need to use multiple measurements and average the resulting images. Furthermore, clinical applications of ASL have been limited by the lack of uniformity, not only in the labeling schemes employed, but also in the readout sequences and quantification models used [11].

According to the labeling scheme, there are two major approaches for ASL, Pulsed Arterial Spin Labeling (PASL) and Continuous Arterial Spin Labeling (CASL). The primary difference among these ASL categories is the technique that magnetically tags the inflowing blood [1]. In CASL, arterial blood water is continuously and selectively labeled as it passes through a labeling plane, typically applied at the base of the brain [5, 12]. Labeling of all blood water occurs at the same location and can be applied for several seconds, maximizing the effects on brain signal. On the other hand, PASL uses a short RF pulse to instantaneously invert blood as well as tissue, and can be applied either below the brain, or to the entire brain with subsequent selective inversion of the imaging slices, to produce a magnetization difference between blood and brain water [13, 14].

However, more recently, a new approach that combines the advantages of the two major ASL techniques described above was developed and named pseudo-continuous arterial spin labeling (pCASL) [15]. This technique was designed to address limitations and technical challenges encountered in the first ASL methods. PCASL is an intermediate technique between continuous and pulsed ASL, which employs a train of discrete pulses to mimic continuous tagging. It was recently established as the optimum ASL labeling

strategy by the ISMRM perfusion study group and the European consortium for ASL in dementia [11]. Additionally, a recommended implementation protocol was described for standard measurements.

Previous work developed in-house and in collaboration with the Center for Magnetic Resonance Research from the University of Minnesota Medical School compared different continuous ASL techniques, including pCASL [16]. In the former study, the inversion efficiency of pCASL was computed through simulations using the Bloch equations. Additionally, the optimal values of gradient strength, gradient moment and flip angle (FA) were also assessed. Discrepancies between simulated and experimental values suggest that the optimal values found in simulations might not correspond to the optimum values for experimental measurements, likely due to hardware imperfections.

The current master thesis project aimed to continue the development and optimization of the pCASL sequence used in the study mentioned above. Specifically, an experimental optimization was performed based on the results of perfusion measurements in healthy volunteers. Considering the tremendous effort necessary for a detailed experimental optimization of all pCASL parameters, only the following were addressed in this study:

1) Determination of the optimal bandwidth and flip angle of the inversion pulses;
2) Implementation of Background Suppression (BS) with different degrees of efficiency;
3) Comparison of balanced and unbalanced pCASL and readout sequences, namely Echo Planar Imaging (EPI) and True Fast Imaging with Steady- state Precession (TrueFISP);
4) Evaluation of the quality of perfusion images obtained with two different head coils.

1.2 Thesis Outline

The thesis presented is divided into nine chapters, the current one (Introduction) included. The remainder of this thesis is organized as follows: Chapter 2 provides some background regarding the physics of MRI; Chapter 3 presents an overview of ASL techniques, specifically a description of the labeling approaches, advantages, limitations and applications of ASL; Chapter 4 goes into detail regarding the pCASL sequence and the

parameters to test; Chapter 5 describes the methods for the experimental optimization, both the experimental settings and post-processing steps; The results are displayed in Chapter 6 and their analysis and discussion in Chapter 7; Conclusions and future improvements are presented in Chapter 8 and Chapter 9, respectively.

The appendixes constitute additional results and an Abstract submitted to the ISMRM 2015 Annual Meeting.

Chapter 2

Magnetic Resonance Imaging

Magnetic Resonance Imaging (MRI) is a medical imaging technique that combines strong magnetic fields and RF signals to generate an image of internal body structures. It became an essential tool to investigate the anatomy and physiology of healthy and diseased individuals [17, 18]. The great versatility of MR techniques available allows measuring parameters such as perfusion, diffusion, brain activation, blood flow velocity and metabolite concentration and was one of the main reasons for the increase in popularity of MR over the last decades as a research and diagnostic tool [10, 19].

Magnetic resonance is based on the fact that every element with a nuclear spin placed in an external magnetic field can be excited to a higher energy level, by absorbing photons at a specific frequency [21]. The excited elements return to the equilibrium state and release the absorbed energy as photons. The emitted electromagnetic signal gives information about the physical and chemical properties of the excited elements [22, 23].

2.1 MRI Physics Overview

At a fundamental level MRI is based on the physics of proton Nuclear Magnetic Resonance (NMR). The biological tissues are made of atoms, mainly hydrogen and carbon which have magnetic properties that make them susceptible to a magnetic field [24]. Since the hydrogen nuclei are the most abundant in biological systems, both in water and macromolecules, such as proteins and fat, clinical MRI focuses on these nuclei [17].

2.1.1 Spins

An atom is a neutral particle that consists of a nucleus and an electronic shell. Both particles in the nucleus (protons and neutrons) possess a quantum property named spin, which is the particle intrinsic angular momentum. In most nuclei, the spins from protons and neutrons are aligned randomly and consequently cancel each other [19]. However, in

nuclei with unpaired neutrons and protons the cancellation is not possible, generating a net spin and a net magnetic moment. Only nuclei with such properties are of interest for MRI.

From all chemical elements, Hydrogen is the most prevalent in the human body and possesses the least complex nucleus, a single, positively charged proton. Besides its high abundance, hydrogen also has the highest gyromagnetic ratio (γ) making it ideal for MRI [17, 25].

2.1.2 Nuclear Spins in the Presence of an External Magnetic Field

When nuclei with an odd number of protons are exposed to a magnetic field, the spins align themselves with the external magnetic field (B_0). As a matter of fact, individual nuclei do not actually align themselves perfectly with the external magnetic field but rather precess around the axis of the field.

According to the Zeeman effect there are two possible situations: the spins can align parallel or anti-parallel to the external field (see **Figure 2.1**) [19]. Naturally the preferred state of alignment is the one that needs less energy, meaning more protons will align parallel to the field. The excess of spin magnets in one direction adds up to a macroscopic effect called net magnetization [19, 25].

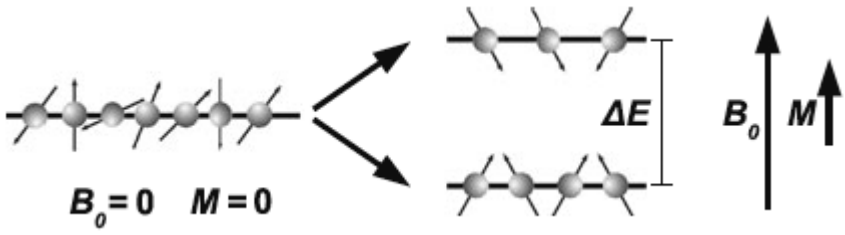

Figure 2.1 – Representation of the Zeeman effect. In the absence of a magnetic field all spins have the same energy and are oriented randomly **(left)**. In the presence of an external magnetic field, the spins align with the field or against it **(right)**. Nuclei that are aligned with the field are more stable and have lower energy than those that are aligned against it. The energy gap generates a macroscopic magnetization (M) [19].

However this magnetization cannot be detected as long as it is oriented in the direction of the external field (B_0) [17]. In order to be able to measure the signal, a rotating magnetic field is applied (RF pulse), which exerts a perpendicular torque on the magnetic moment

causing it to rotate away from the direction of the magnetic field B_0. Similar to a spinning top, the magnetization continues to process about the axis of the external field. (see **Figure 2.2**) [17, 25].

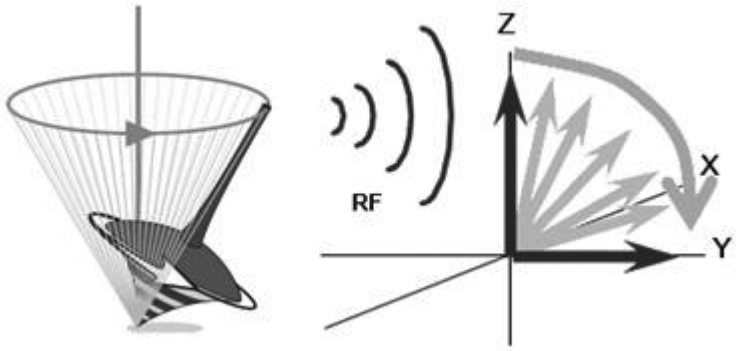

Figure 2.2 – (Left) Spins precess around the direction of the magnetic field at a certain frequency similar to a spinning top. **(Right)** A RF pulse with Larmor Frequency excites the spins, flipping the magnetization toward the x-y plane [17].

The precession frequency is not constant, it depends upon the strength of the magnetic field, the stronger the magnetic field, the faster the precession rate. The oscillating frequency of the RF pulse is calculated using the Larmor equation (see equation **2.1**) and has to match the Larmor frequency (ω) of the spins to cause the effect of resonance [17].

$$\omega = \gamma B_0 \qquad \textbf{2.1}$$

By applying RF pulses of exactly the Larmor frequency, the spin ensemble loses its equilibrium. This happens because the RF pulse has the same frequency as the spins, which allows an exchange of energy between both. This way, some protons absorb energy and transit to a higher energy state, causing a decrease in the magnetization in the direction of B_0 [25]. In addition, the RF pulse causes the protons to precess in phase (same direction at the same time) and thus their magnetic vectors add up and the resulting magnetic vector points in the direction of the flip angle, establishing a transverse magnetization (M_{xy}). The transverse magnetization can then be detected by its induction effect on a nearby coil and corresponds to the MRI signal that we detect [17].

2.1.3 Spin Relaxation

Since the application of a resonant RF pulse disturbs the spin system, there must subsequently be a process of returning to equilibrium. This process is called relaxation and is caused by the exchange of energy between the spin system and its surroundings or interactions between spins [17].

Once the RF transmitter is turned off, the spins start to return to their initial alignment with the B_0 magnetic field. The first process of relaxation, named spin-lattice relaxation, is related to the process of realignment to the external magnetic field. It corresponds to the rate at which the M_z component recovers its initial magnetization M_0 and is characterized by the longitudinal relaxation time T_1 [26]. The source of T_1 relaxation are local magnetic field fluctuations created through molecular motion. Magnetic field fluctuations in the range of the Larmor Frequency show the strongest effect and cause the protons to change their spin state [17, 19].

The second process, faster than the first one, is characterized by the spin-spin relaxation time T_2 (decay of the transverse magnetization). Directly after the RF pulse, the spins are phase-coherent. They act like one large magnet that rotates in the x-y plane. However, the rotating spins lose their coherence due to unavoidable interactions, the spins get dephased and the transverse magnetization begins to decay [19]. The T_1 and T_2 constants depend on the tissue, that is, they are tissue-specific [27]. Both processes of spin relaxation are represented below in **Figure 2.3**.

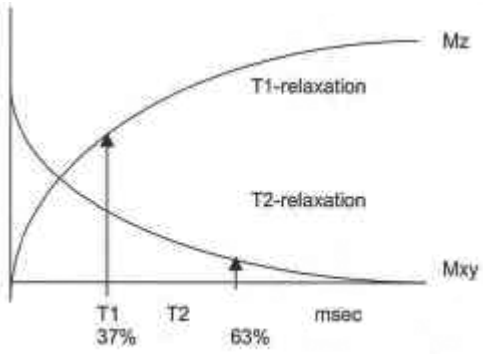

Figure 2.3 – Diagram of T_1 and T_2 relaxation times [28].

However, in experimental studies the transverse magnetization decays at a rate faster than T_2. This loss of signal is caused by inhomogeneities in $B_{0,}$ since in a real system, the static magnetic field as felt by the spins is not the same everywhere. Due to variations in the magnetic fields experienced by the individual spins, their precession frequencies differ, causing them to fan out. The superposition of all spins forming the macroscopic magnetization will therefore decay and disappear. This process is characterized by T_2* decay and known as apparent transverse relaxation time [17, 19].

2.1.4 Signal Detection

During relaxation, the magnetization vector is still precessing around the static magnetic field, which induces an alternate magnetic field and consequently according to Maxwell's equations, it also induces an alternating electric field. Additionally, in accordance with Ohm's law this creates an alternate electric current that corresponds to the magnetic resonance signal detected by the receivers coils and is named Free Induction Decay (FID) [29].

Furthermore, since the FID is decaying immediately after the RF pulse, measuring its strength is difficult [17]. For that reason, echoes are the preferred signals for imaging. In section 2.1.7 the mechanisms leading to echoes generation are further explained.

2.1.5 Spatial Encoding

The signal detected contains information about the entire volume excited. Without a spatial allocation, we cannot distinguish the different tissue structures. To create an image, it is necessary to extract information about the location of the protons, only possible via spatial encoding [17].

The common method to add spatial differentiation is to spatially vary the magnetic field using switching gradients. The nuclear spins will then show different precessional frequencies at different positions. This can be achieved in three steps: slice selection, phase encoding and frequency encoding, with the application of magnetic field gradients in the three orthogonal directions generated by three independent sets of coils. The gradients will

cause a change in the magnetic field in a certain direction, specifically, a linear increase or decrease of the field [30].

In slice selection, a gradient is switched (in the z-axis) simultaneously to the RF pulse. The principle of slice selection is the following: if the Larmor frequency changes with position, a RF pulse with a single frequency only selects those spins that are at the appropriate position where the Larmor frequency is equal to that of the pulse [22]. However, in order to achieve a certain resolution in the z-axis, the RF pulse has a defined bandwidth, that is a range of frequencies of the pulse that will excite a given volume. In this manner, the RF pulse can stimulate the desired spatial area of the slice thickness. A transverse magnetization (and therefore an MR signal) is generated only within the selected slice. Changing the frequency of the pulse modifies the position of the excited slice, while its thickness is determined by the bandwidth. The slice position thus depends on the strength of the gradient and the pulse frequency [30].

To acquire information of the individual points in one image within a slice, another two gradients are used that enable the encoding of the two remaining dimensions, the frequency and phase encoding gradients.

During the time between the RF pulse and the readout, a gradient in the y direction is switched on briefly. As a result, the spins will precess at different speeds for a short time. After the gradient is switched off, the spins along the resolved direction will show different phase shifts directly proportional to their locations. This gradient introduces a spatially varying phase on the entire acquired signal. Changing the duration of the temporary gradients allows the acquisition of signals with different phase encoding [24].

If we switch the direction of the gradient to the x-axis during readout, the spin ensemble of the individual voxels precesses along the direction of the gradient at an increasing frequency [25]. Therefore, this gradient introduces a spatially dependent frequency that differentiates pixels within the same phase encoding. Similar to spectroscopy, a Fourier transformation then recovers the frequency and, accordingly, the spatial information [30, 31].

2.1.6 K-space

The image is not directly produced through the measurement procedure. Instead raw data is generated as a first step from the MR signals received. The image is afterward computed from the raw data.

The phase and frequency information are stored in k-space, where each row corresponds to the frequency information and each column corresponds to the phase information. The image construction is done by calculating the 2D inverse Fourier Transform (FT) of the samples collected in k-space [17, 30].

2.1.7 Spin Echo and Gradient Echo Sequences

As displayed in section 2.1 echoes are the preferred signal for MRI. We will only discuss the two most common methods for echo generation, spin echo (SE) and gradient echo (GE) sequences.

To generate a basic SE, an excitation pulse with a flip angle of 90º or less is followed by a second pulse with a flip angle of 180º (see **Figure 2.4**). By means of the 180º pulse, the spins are flipped and rephased generating a new MR signal, the spin echo. The time between the first excitation pulse and the generation of the maximum value of the echo is called echo time (TE) [17, 30].

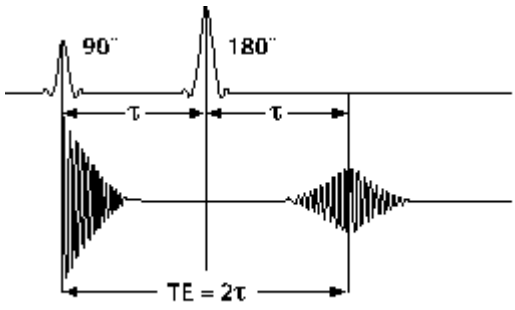

.

Figure 2.4 – Spin echo sequence diagram [17].

As hinted by the name, in GE sequences the echo is generated by a gradient (see **Figure 2.5**). Instead of applying an additional RF pulse after the 90º excitation pulse, a change in the magnetic field is introduced by turning on a gradient [32].

Since the precession frequency of the spins is directly proportional to the field strength, the spins will rotate at different speeds along the field change. When a gradient pulse is turned on directly after the RF pulse, it will artificially dephase the spin frequencies. Since the spins will rotate at different speeds, they lose their phase quicker [30]. The FID is destroyed considerably faster than it would be under normal circumstances.

By reversing the polarity of the gradient, the spins will be in-phase again, that is, they are rephased. We measure an echo during the rephasing of the FID. This means that we do not cancel the static T_2* dephasing mechanism as in spin echo techniques. Instead, the use of gradient pulses quickly destroys the FID and rebuilds it again, all within the T_2* decay [17]. The echo time for a GE has to fit into the T_2* time, therefore GE techniques are faster than SE procedures. To generate gradient echoes, the flip angle of the stimulating RF pulse is usually less than 90º. The main advantage of this approach comprise reduced measurement times [33].

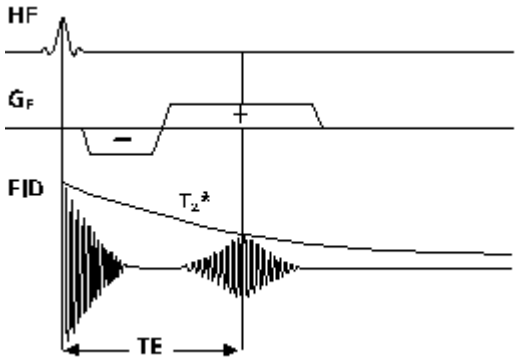

Figure 2.5 – Gradient echo sequence diagram [17].

2.2 Image Quality

Image quality is dependent on complex interactions between the spatial resolution of the structures acquired in the image, signal strength, contrasts and noise [31].

2.2.1 From Signal to Image

The MR image consists of a multitude of image pixels. This configuration is known as image matrix. The pixels in the image represent the individual volume elements (voxels) in the slice and each have a specific grey value [31].

After the RF pulse stimulates a slice in the patient's body, each voxel in that slice emits an MR signal. Among other things, the signal strength depends on the quantity of signal-generating proton spins in the respective voxel (proton density) which means the more spins contribute to magnetization, the stronger the signal [34].

The more pixels are in an image, the more image information is available. This means the image has a higher resolution.

2.2.2 Tissue Contrast

The raw data signal acquired from the slice is a mixture of the individual voxel signals. The MR image is computed from the raw data signals using FT [34]. In this manner, signal intensity can be assigned to each voxel and therefore a respective grey value.

Bright pixels in the image represent stronger signals, weaker signals result in darker pixels. The contrast in the image is, simply put, the difference in signal strengths between different types of tissue, since each type of tissue emits individual signal strengths, allowing for anatomical differentiation in the image [18, 31].

The differences in the MR signal depend on tissue-specific parameters, such as the T_1, T_2 and proton density of the tissues. Furthermore, the effect of the tissue-specific parameters on the contrast can be concealed or enhanced by a set of sequence parameters, i.e., the time between consecutive excitation pulses, known as Repetition Time (TR), TE and flip angle. For short TR and TE, the contrast in the image will be potentiated by the difference in T_1 value of the tissues, alternatively, using long TR and TE, the contrast will be dependent on T_2 differences [1].

2.2.3 Signal versus Noise

The signal measured is not solely the signal emitted from the protons in the imaged area. There are additional sources generating an undesired signal called noise. In other words, noise is an unwanted occurrence in the MR image that is superimposed on the MR signal and appears in the image as a grainy, random pattern [35]. This phenomenon has an adverse effect on image quality and represents statistical fluctuations in signal intensity that do not contribute to image information.

The MR signal is emitted by the selected slice and/or the respective voxel. On the other hand, noise has two sources, one is the signal generated throughout the human body due to the molecular motion of charged particles, known as the Brownian motion and the other is the electronic noise of the receiver technology [31]. These additional sources of unwanted signal can be problematic when the signal from the slice is too weak.

The SNR is an important criterion to evaluate image quality, since it accounts for noise contributions on the image. This parameter provides a direct means for comparison of signals obtained with different imaging methods and represents a quantitative measure of image quality. A higher SNR is a sign of improved image quality [31].

2.2.4 Amplifying the Signal

It is not possible to completely suppress noise from images. However, the signal can be amplified. A strong signal is therefore the first step towards good image quality [34].

One way of amplifying the signal consists of increasing the voxel size using a larger slice thickness, because the signal measured is proportional to the voxel size. However, increasing slice thickness reduces spatial resolution and might originate partial volume effects that distort image results. Alternatively, the SNR can be enhanced through multiple measurements of one slice (several acquisitions) and posterior averaging of the results in a single image [36]. Nevertheless, this way the SNR does not increase in a linear fashion, it is instead proportional to the root of the number of acquisitions.

Chapter 3

Arterial Spin Labeling

Arterial Spin Labeling is an entirely non-invasive method to measure perfusion in vivo. Perfusion refers to the delivery of oxygen and nutrients to a capillary bed in the tissue by means of blood flow, and is one of the most fundamental physiological processes. Abnormalities or disruption in this process can have heavy effects, especially in the brain, a particularly highly perfused organ that receives a large portion of cardiac output (about 20% under normal conditions) [1]. Therefore, cerebral perfusion imaging has an important role in the diagnosis and evaluation of different brain disorders, as well as in examining brain function.

In comparison to more established radionucleotide methods such as positron emission tomography (PET), ASL has been shown to have improved spatial and temporal resolution and is non-ionizing [37]. Furthermore, ASL offers an alternative to Dynamic Susceptibility Contrast (DSC) MRI, since the usage of gadolinium based contrast agents is not recommended in patients with kidney failure [38].

3.1 Brain Perfusion

The brain can be roughly divided in three types of tissue; gray matter (GM), white matter (WM) and cerebrospinal fluid (CSF). The outer surface of the brain, also known as cortex, consists of GM, which surrounds an inner mass of WM (see **Figure 3.1**). The GM comprises mainly neuronal cell bodies, dendrites and capillaries, while WM is composed of myelinated axons.

As mentioned above, the brain receives a considerable portion of the cardiac output. This happens due to the high metabolic demand necessary to support the electrical and chemical activity that forms the basis of neuronal communication. In fact, 20-25% of the total oxygen and glucose consumption of the body goes to the brain and 95% of that goes specifically into the gray matter [39], hence the high values of perfusion found in GM.

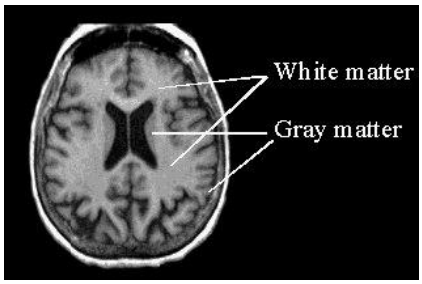

Figure 3.1 – White and Gray matter in a cross section of the brain [40].

Cerebral Blood Flow (CBF) reflects the amount of blood perfusion in the brain, often defined in ml of blood per 100 gram of brain tissue per minute [41]. The typical CBF values for the whole brain are 40-60 mL/min/100 g and for gray matter, CBF values in range of 40-100 mL/min/100 g are considered normal [11].

3.2 ASL Principles

Essentially, ASL uses arterial blood water as an endogenous diffusible tracer by inverting the magnetization of the blood using RF pulses [5, 12]. This way, the hydrogen protons are magnetically labeled as they flow through the internal carotid artery (ICA) and vertebral artery (VA), which are the major feeding arteries of the brain. The labeled protons exchange with the water protons in brain tissue as the blood flows into the capillary. After a delay to allow for labeled blood to flow into the brain tissue, labeled images are acquired that contain signal from both labeled water and static tissue water [42]. Separate control images are acquired without prior labeling of arterial spins. Control and labeled images are subtracted, eliminating the static tissue signal (see **Figure 3.2**). The remaining signal is proportional to CBF and consists of the amount of labeled blood from arteries delivered to the tissue by perfusion in arbitrary units (a.u.). The signal difference is usually a fraction (1-2%) of the tissue signal. Multiple control and label images are acquired to ensure sufficient SNR [1]. An absolute quantitative perfusion map can be obtained using quantification models, such as the General Kinetic Model [43].

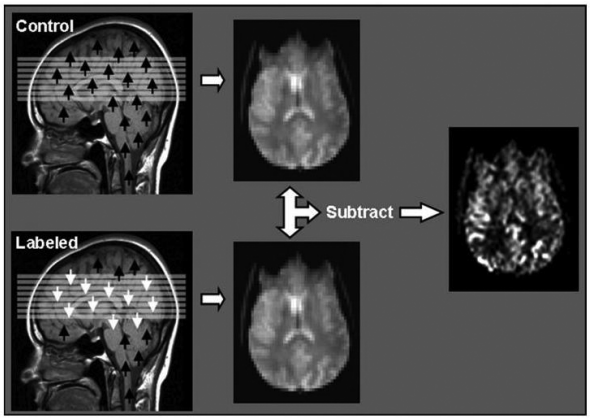

Figure 3.2 – Arterial blood is tagged and, after a delay, flows into the imaging plane, during which time the label decays with T_1. Snapshot images are acquired in labeled and control conditions and subtracted, yielding a difference image with signal intensity proportional to CBF [10].

Thus, the principle behind the ASL techniques is to distinguish the net magnetization of arterial blood water flowing into the brain from the net magnetization of brain water. As the labeled water flows through the brain, a net decrease in magnetization is obtained due to the mixing between the existing local magnetization and the one from the freshly arrived labeled water, which is proportional to the flow rate. Therefore, this decrease in magnetization may be used to calculate CBF [7].

The lifetime of the labeled signal is determined by the longitudinal relaxation time of blood, which is in the range of 1300-1750 ms at clinical field strengths [44, 45]. This time interval is similar to the transport time from the labeling region to the tissue of interest, known as the arterial transit time (ATT). The ATT places constraints on the choice of an appropriate delay, since a short delay does not allow for complete delivery of the labeled blood water to the tissue, whereas a long delay results in strong T_1 decay and therefore reduced SNR. The ATT varies between individuals, regionally, and between healthy and pathological tissue [46].

3.3 Labeling Strategies for ASL

Labeling of the arterial blood can be accomplished with a number of different strategies. The most common methods are CASL and PASL. Despite some differences,

any ASL sequence is basically made up of two distinct and independent components, a preparation component and an acquisition component. The preparation component labels the inflowing blood in different magnetic states for the control and label images. The acquisition component acquires the data. These two components are usually separated by a delay time to allow the label to reach the tissue of interest [7]. There may be some variations, such as additional pulses to shape the input function before the acquisition part or use of additional coils, but the structure of the sequence remains the same.

The original strategy for labeling the arterial blood water is known as CASL, which attempts to continuously label blood as it passes through a region known as labeling plane [5, 12]. Later, a new labeling scheme of arterial spin labeling pulse sequences was proposed, termed PASL, that employs a single pulse to define a volume and label the containing arterial blood [13, 14]. Pulsed and continuous ASL labeling methods differ fundamentally in both the spatial extent and the duration of the labeling (see **Figure 3.3**).

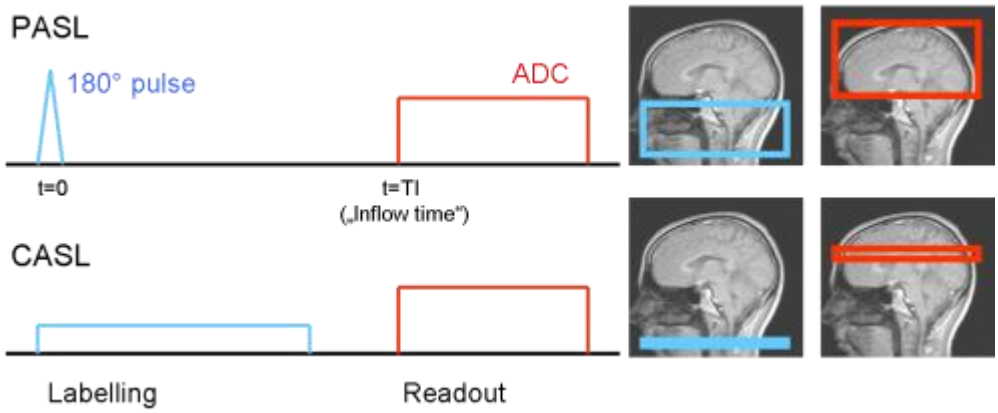

Figure 3.3 – Schematic representation of an ASL sequence and corresponding label and imaging regions. PASL uses a single short pulse with a total duration of 10–20 ms, to invert a thick slab of arterial water spins. For CASL, labeling occurs over a long period, typically 1–3 s, as blood flows through a single labeling plane and is inverted [47].

More recently, based on conventional PASL and CASL labeling approaches, an intermediate method termed Pseudo-continuous ASL was proposed [48, 49]. PCASL utilizes a train of discrete RF pulses to mimic continuous tagging that is often unavailable on imagers due to the requirement of continuous RF transmit capabilities. PCASL has the potential of combining the merits of PASL, including less hardware demand, and CASL,

which consist of a longer tagging bolus and thus higher SNR. These improvements provide a better balance between tagging efficiency and SNR [48, 49].

3.3.1 Pulsed Arterial Spinning Labeling

PASL methods have been the most widely used in ASL to date because of their ease of implementation and low specific absorption rate (SAR). Several approaches have been proposed for PASL using a single short inversion RF pulse and generating two images, in which arterial blood water has an opposite magnetization state. Typically, a slab containing the arterial supply to the organ of interest is labeled with a short RF inversion pulse, followed by a delay to allow the inverted spins to flow from that slab into the tissue of interest. Various methods were presented that differ in the location of the labeling plane and the choice of the labeled state of blood for control and labeled images [7]. From the variety of PASL methods available, flow-sensitive alternating inversion recovery (FAIR) and signal targeting with alternating radiofrequency (STAR) were the first implementations suggested. The first, FAIR, uses slice-selective inversion of the imaging slices as label condition and a non-selective inversion pulse of the whole region as control condition [14, 50], while the second method, STAR, uses a slice selective inversion below the imaging slices as label condition, and no RF pulses for the control state [13].

The major advantages of PASL are the high labeling efficiency and the low SAR. As a drawback, the SNR of the perfusion-weighted images isn´t as high as in CASL and PASL suffers from additional difficulties in quantification.

3.3.2 Continuous Arterial Spinning Labeling

In the continuous approach (CASL), the spins are continuously inverted at a plane inferior to the brain by long pulses of low power and the MR signal change is measured as the inverted protons diffuse into the tissue of interest. Usually, the inversion plane is located below the circle of Willis, where the arterial supply to the brain is perpendicular to the labeling plane [5, 12]. Both for CASL and for pCASL the inversion of the spins is achieved through flow-driven adiabatic inversion. The mechanisms involved in this inversion are explained in section 3.3.2.1.

The implementation of CASL is limited by hardware constraints, but the perfusion signal is much stronger than PASL's signal, consequently CASL yields a higher SNR [43]. Since the time between label and imaging is long in CASL, the perfusion signal is more homogenously distributed, resulting in the perfusion signal becoming less sensitive to ATT [1].

The main drawbacks of continuous ASL are the long inversion pulses for labeling purposes, which produce a significant amount of magnetization transfer (MT) at the tissue of interest, and also the large amount of RF energy deposition in the subject, resulting in a higher SAR [37, 51]. Briefly, magnetization transfer consists of signal loss due to preceding off-resonance RF pulses [51].

Due to MT, subtracting a tagged image from a control image would create an image not only of the perfusion effects, but also of the degree of magnetization transfer, leading to inaccurate quantification [1]. Several strategies to overcome the magnetization transfer problem have been tried, however, some solutions have limited the technique to the measurement of a single slice [52]. To overcome the single-slice limitation, a sinusoidal modulation of the RF labeling waveform during the control while keeping the frequency offset the same as the labeling's was proposed. The application of such an RF pulse simultaneously with a gradient will continuously invert two planes at the same time, theoretically leaving the net magnetization of the arterial blood unaltered. The power of the amplitude modulated control is configured to produce an identical MT profile in the brain during the tag and control imaging stages, allowing multi-slice acquisitions [3].

.

3.3.2.1 Adiabatic Inversion

In CASL, inversion of blood water in the feeding arteries is accomplished using flow induced adiabatic inversion. The adiabatic inversion operates under the adiabatic fast passage (AFP) principle, according to which a magnetization vector initially parallel to the effective magnetic field follows the direction of the effective field, as long as the field does not change its direction to a great extent during one rotational period of the magnetization about the effective field [52, 53].

The AFP principle is applied for labeling the arterial spins as will be explained in the next paragraphs. In order to select the labeling region, a long RF pulse is applied at some

frequency offset and in the presence of a slice-selective gradient. These pulses will have different effects on spins. When applied to stationary spins at the labeling plane, they become saturated and lose phase coherence, but when applied to spins moving through the labeling plane they experience a gradual change of their resonance frequency, since the former is proportional to the magnetic field [2]. As the spins move through the inversion plane, they are moving along a gradient that sweeps their frequency from above resonance to below the resonance frequency of the applied RF pulse. Therefore, the difference between the resonance frequency of the protons and the transmission frequency changes from positive to negative and is zero at the center of the labeling plane [52, 53]. Because of this effective "frequency sweep", the magnetization experiences a rotation from pointing along the direction of the main magnetic field to pointing against it (+z to –z axis) [54]. As the protons move through the inversion plane, the "effective" field to which they are locked rotates from pointing along the direction of the main magnetic field to pointing against it. Consequently when the flowing spins leave the plane, their magnetization is inverted. This phenomenon is known as flow induced adiabatic inversion [2].

One major advantage of this inversion technique is that the AFP condition is maintained over a range of blood flow velocities, in such a way that small variations in flow velocities, originating from physiological conditions or the pulsatile nature of blood flow, are well tolerated [55].

3.3.3 Pseudo-Continuous Arterial Spinning Labeling

More recently a new approach to CASL, termed pseudo-continuous ASL or pulsed-continuous ASL (pCASL), was introduced, easing the technical restrictions of CASL [48, 49]. Pseudo-continuous arterial spin labeling has been demonstrated to provide the sensitivity of the continuous arterial spin labeling method while overcoming not only the restrains of the duty cycle but also the MT effects.

This adaptation of the CASL technique consists in breaking up the continuous labeling pulse into a train of pulses applied in rapid succession, in the presence of an optimized gradient shape to achieve the same adiabatic inversion effect [49] . In the control case, however, the same pulse train is applied but the phase of every other pulse is shifted by 180 degrees, such that it cancels the flip of the previous pulse. The end result is that both

the control and the labeled image receive the same amount of magnetization transfer, the flowing blood's magnetization gets inverted prior to collecting the labeled image but it remains un-inverted during the collection of the control image.

The caveat is that pCASL is sensitive to magnetic field inhomogeneity (off-resonance) at the inversion plane. This effect can severely affect the efficiency of the labeling process, crippling the technique, and is exacerbated at higher magnetic fields.

PCASL is considered the best method to approach continuous labeling studies because of its appealing properties, essentially, being able to provide high inversion efficiency, multislice capability and broad compatibility with existing scanner hardware [11].

3.4 ASL Applications

ASL has substantial interest for studies of various brain disorders, including chronic and acute cerebrovascular diseases, brain tumors, neurodegenerative diseases such as Alzheimer's disease, as well as other kinds of dementia, and for examination of brain function [8]. In addition, due to its non-invasive nature, this method has gained increased popularity in studies with children [10, 52]. Furthermore, in patients with cognitive decline and Alzheimer's disease, arterial spin labeling perfusion measurements may be used to detect early changes in regional hemodynamics before structural changes become apparent. Even though the precise mechanisms between tissue blood supply and glucose metabolism, which allow regional brain activity to be assessed, are still not completely understood, perfusion measurements with ASL have been used to study a wide range of physiological functions due to the close coupling between the two variables referred above [8, 12].

3.5 ASL Limitations

The low SNR of the ASL measurements is arguably the main reason for its relatively limited use. Furthermore, motion is the most commonly seen artifact in ASL measurements. In the presence of motion artifacts, subtraction does not eliminate signal from static tissue, leading to an incorrect CBF quantification.

More recently, clinical applications of ASL have demonstrated the challenges of optimizing sequence timing, in particular the post-labeling delay to allow all labeled blood

to enter the microvasculature while not losing too much signal to T_1 decay because of excessive wait times [57, 58]. While measurement of ASL signal at multiple delay times is an option, it causes reduced SNR per unit of time.

Another constraint in ASL imaging is the need for fast image acquisition, to ensure that the signal from the labeled blood is measured before it relaxes to equilibrium. This makes rapid single-shot interleaved tagged and control imaging methods such as EPI ideal for ASL measurements. However, fast imaging is done at the expense of spatial resolution, which might give rise to partial volume effects [59]. Additionally, scanner stability is crucial for reliable ASL measurements, as perfusion is obtained through averaging over the time course.

Chapter 4

Pseudo-Continuous ASL Sequence Specifications

4.1 pCASL Sequence

A typical pCASL sequence (see **Figure 4.1**) has three components, the labeling, post labeling delay and readout. The labeling is achieved by a train of rapidly repeated low tip angle RF pulses in combination with magnetic field gradients with alternating polarity, mimicking the effect of continuous labeling. The readout scheme can be chosen according to the purpose of the study, however, for pCASL fast readout sequences such as EPI are preferred, to prevent signal loss due to T_1 decay [7].

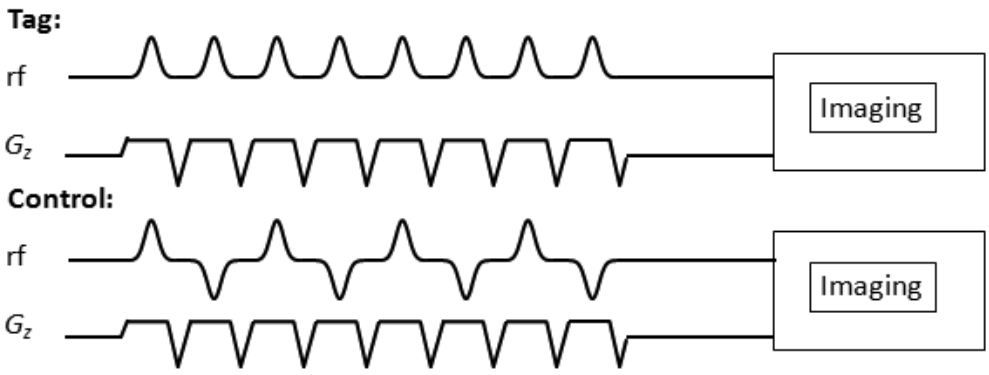

Figure 4.1 – Pulse diagrams and label/control geometries for pCASL. Repeated RF pulses create a pseudo steady-state, mimicking the continuous inversion of CASL. The label is applied for a long period of time through a train of pulses applied in rapid succession to achieve flow driven inversion. In the control case, the same pulse train is applied but the phase of every other pulse is shifted by 180 degrees, in order to cancel the flip of the previous pulse [16].

4.2 Balanced and Unbalanced pCASL

Concerning the gradient moment, pCASL has been implemented in two different ways, balanced and unbalanced [15, 60]. Both methods apply an RF pulse train with alternate polarity in control scans and constant in tag scans. The difference between the

methods is in the gradient moment per cycle (see **Figure 4.2**). In the balanced implementation, tag and control scans share an identical gradient waveform with a residual net moment per cycle (i.e. net moment per cycle is nonzero for both tag and control). This residual gradient needs to be adjusted to generate inversion in tag sessions and maintain unperturbed M_z in control sessions [60]. On the other hand, for the unbalanced method the gradient moment per cycle is nonzero in tag and zero in control acquisitions [15, 48].

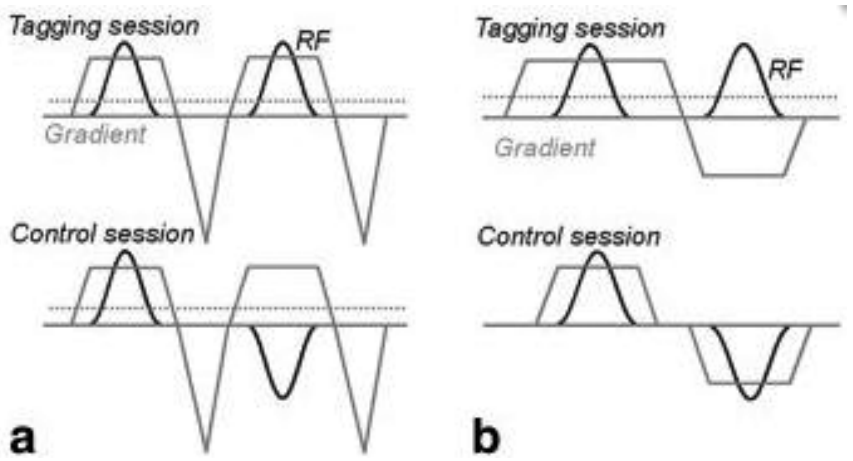

Figure 4.2 – Representation of two pseudo-continuous tagging schemes, balanced **(a)** and unbalanced **(b)**. In both methods, the polarity of the RF pulse is constant during tagging and alternated during control. In the balanced method the gradient moment between two consecutive RF pulses is identical in tagging and control, both nonzero, but in unbalanced method it is different, being nonzero for tagging and zero for control [48].

Previous studies showed that the unbalanced approach is less sensitive to resonance offset than the balanced method, in which tag and control gradients change simultaneously. However, the use of different gradient waveforms in tag and control sessions makes the unbalanced method more susceptible to artifacts caused by eddy currents with long time constants. Nevertheless, in general, the results obtained with the two schemes have a comparable performance [48].

4.3 Background Suppression

In ASL, perfusion images are obtained through the subtraction of tag and control images. Naturally, if images of the same volume are acquired under identical conditions

they should have matching static tissue signal, which would be eliminated when performing the subtraction. However, any movement between the acquisition of the pair tag/control results in spatial misregistration, which can degrade image quality and cause misleading artifacts [3]. Subject motion is, in general, the dominant noise source in ASL. The subject's motion produces signal fluctuations that are proportional to the signal intensity in the control and tag images. In theory, it is possible to decrease the signal intensity of the unsubtracted images without a proportional decrease in the ASL difference signal, consequently improving substantially the overall SNR of the ASL measurements [61, 62]. The decrease of the background tissue signal can be accomplished using a combination of spatially selective saturation and inversion pulses, referred to as background suppression (BS). Employing BS can markedly improve temporal SNR, which is of particular value in clinical ASL [63].

The suppression of the static tissue signal is accomplished through the use of an initial saturation pulse selective to the imaging region followed by carefully timed inversion pulses, so that the longitudinal magnetization of static tissue passes near or through zero at the time of image acquisition (see **Figure 4.3**) This way, the blood flowing through the labeling plane does not experience the initial saturation, but does experience the inversion pulses. For perfect inversion pulses, each inversion changes the sign of the ASL label/control magnetization difference, but nominally does not affect the magnitude of this difference [63, 64].

Several inversion pulses can be implemented, the larger the number of inversion pulses, the more accurately static tissue can be suppressed over a wide range of tissue T_1 values. However, since the efficiency of the inversion pulses is not perfect, each inversion pulse reduces the ASL signal. Generally, two pulses can be considered a good trade-off. Another aspect is that BS only nulls the magnetization of static tissue at one point in time, after which the magnetization of static tissue continues to grow toward the equilibrium state by relaxation [63]. For methods that require multiple excitations per TR, such as multislice single-shot two dimensional (2D) methods, BS can be optimal for one slice, but is progressively less efficient for other slices. Nevertheless, BS achieved through the application of multiple inversion pulses has become an attractive tool to improve ASL robustness and SNR [11].

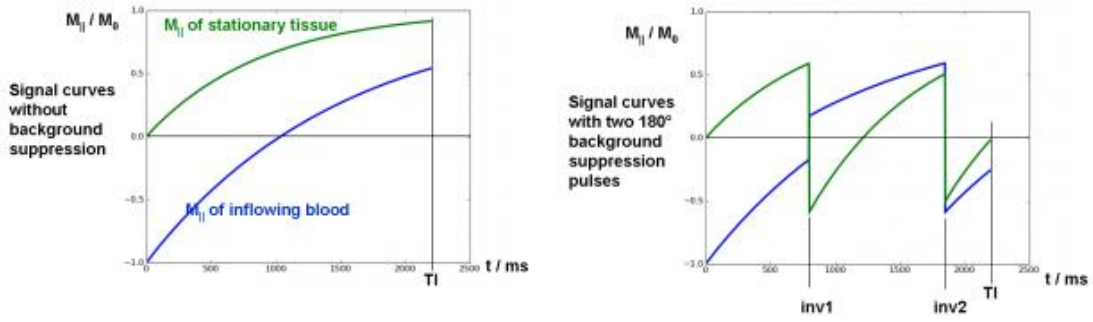

Figure 4.3 – Magnetization curves without **(left)** and with background suppression **(right)**. Additional global inversion pulses are applied between inversion and readout as background suppression pulses. The timing of the pulses is optimized to null the tissue signal with a certain T_1 at the time of readout [65].

4.4 Readout Sequences

Image collection following the labeling component can be achieved in a number of ways, but is important to take into account the goals of the specific application. Normally in MRI, there is a trade-off between SNR, acquisition speed and resolution. In most ASL applications EPI is preferred for acquisitions because of its short duration. Regardless of being the fastest acquisition method, EPI can introduce distortions in regions of high magnetic field susceptibility variations, particularly at the base of the brain [4]. Fast spin echo acquisitions are also a popular readout scheme for ASL, as they are insensible to off-resonance artifacts and can provide relatively high SNR and speed. One example is the single-shot 3D-GRASE (Three Dimensional Gradient Echo and Spin Echo) sequence, which provided an increase in SNR compared to 2D EPI [66] .

Other readout approaches have been attempted for ASL including Rapid Acquisition with Refocused Echoes (RARE) and Gradient Echo Asymmetric Spin Echo (GREASE). They were used to minimize susceptibility artifacts, at the cost of lower temporal resolution, blurring or lower SNR per unit time. Balanced steady state free precession (bSSFP) readout overcomes these limitations while maintaining relatively high temporal resolution and SNR per unit time [67, 68]. Therefore, in our work we implemented this readout sequence and compared it to the standard EPI.

4.4.1 Echo Planar Imaging

EPI is an acquisition method that is widely used in functional Magnetic Resonance Imaging (fMRI) [69]. It is a unique imaging method, particularly suitable for ASL, because it can collect an MR image from a single FID within hundreds of milliseconds. The outcome of such a rapid acquisition is a high temporal resolution and a reduction of motion artifacts. However, EPI is more sensitive to other artifacts than conventional imaging [36].

There are two main categories of EPI, single-shot and multi-shot. Only the single-shot variant will be further discussed since it is the one used in the experimental protocols. The basic idea of single shot EPI is to fill k-space in one shot [36].

EPI consists of a pulse sequence in which multiple echoes of different phase steps are acquired using rephasing gradients (see **Figure 4.4**). This is accomplished by rapidly reversing the readout or frequency encoding gradient. The signal intensity will eventually decay to zero because of T_2 and T_2^* effects.

Figure 4.4 – EPI pulse sequence design [36].

As mentioned before, in EPI multiple lines of imaging data are acquired after a single RF excitation. First, an RF excitation pulse is applied together with a slice selective gradient, in order to excite the desired slice. Thenceforth the frequency encoding gradient oscillates rapidly from a positive to negative amplitude, forming a train of gradient echoes.

In conventional EPI the phase-encode gradient was kept on continuously during the acquisition, resulting in a zigzag or sinusoidal coverage of k-space. However, in more recent approaches called blipped phase encoding, the phase encoding gradient is on briefly, only while G_x is zero. Each echo is phase encoded differently by phase-encoding blips on

the phase encoding axis. Each oscillation of the frequency encoding gradient corresponds to one line of imaging data in k-space, and each blip corresponds to a transition from one line to the next in k-space.

EPI suffers from various artifacts and image reconstruction requires more than just applying a simple inverse FT to the acquired k-space data. Some of the artifacts are caused by inhomogeneities of the static magnetic field, inaccurate timing of readout gradients or eddy currents [36]. With single-shot EPI, any phase error tends to propagate through the entire k-space. Because of the presence of phase error propagation along the phase-encode axis, chemical shift artifacts in EPI occur along the phase-encode axis. These artifacts can be prevented using an effective fat suppression technique. Besides the sensitivity to the artifacts mentioned formerly, EPI has other restrictions such as a limited spatial resolution.

4.4.2 True Fast Imaging with Steady-State Precession

TrueFISP is the Siemens implementation of the bSSFP imaging technique. This sequence utilizes a short TR/TE ($TR<<T_1$ and T_2), high flip angle and a balanced pulse sequence that preserves transverse magnetization, resulting in fast T_1/T_2 weighted images with high SNR and insensitivity to dephasing and signal loss [36].

When a fast acquisition of MRI signals is desired, instead of waiting for a full T_1 or T_2 recovery before the next excitation pulse of the next iteration, a string of RF pulses at alternating phase angles of 0° and 180° to flip the magnetization with minimum possible TR, can be applied rapidly and repeatedly to make the amount of longitudinal magnetization before each excitation pulse constant. This way, the MR signal will never completely decay, and the spins in the transverse plane never completely dephase. A steady-state is reached when the amount of transverse magnetization equals the recovery of longitudinal magnetization during TR. This state can be maintained by an appropriate choice of TR and FA [36].

Additionally, a balanced sequence attempts to undo all dephasing caused by the imaging gradients during the TR, so that a maximum amount of magnetization is preserved, therefore in balanced sequences all image gradients have net area equal to zero during one TR. Consequently, the fully refocused gradients imply that the off-resonance

precession is the primary source of phase accrual. The gradient induced dephasing within a voxel is smaller for SSFP sequences, meaning they are less sensitive to motion [36] .

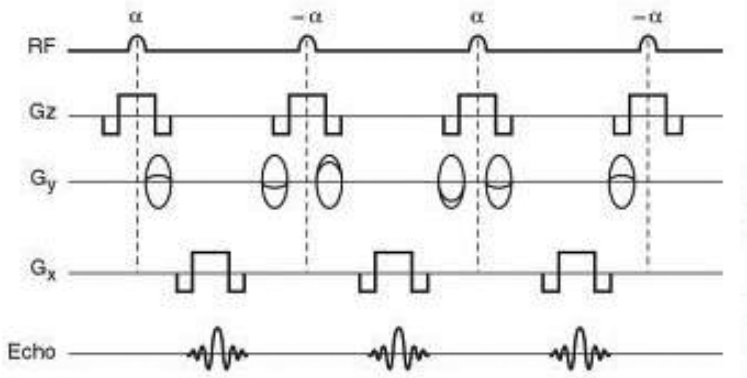

Figure 4.5 – TrueFISP pulse sequence diagram. [36].

In some studies, bSSFP readout scheme (see **Figure 4.5**) was attempted for PASL and PCASL in the body and brain but the feasibility and performance of bSSFP for ASL have not been thoroughly evaluated [68]. A disadvantage of the 2D bSSFP is that it is limited to a single slice. Multiple slice acquisition will increase the total acquisition time proportionally, which is impractical.

4.5 Model for CBF Quantification

A major component in ASL MRI is to obtain quantitative perfusion values from the measured data. However, in order to extract a quantitative measure of perfusion, a detailed model of the process combining kinetics and relaxation is required [70].

ASL is based on the theory of tracer kinetics where the tracer is the endogenous magnetically labeled arterial water. This theory provides the tools to describe the relationship between the arterial concentration of labeled water and the resulting tissue concentration, that were used as the basis of the general kinetic model for quantitative perfusion imaging with ASL [43]. In this model, Buxton adapted the modified Bloch's equations described by Detre et al. to include delivery and clearance terms proportional to blood flow [5].

Since Detre's original quantification model, that assumes the brain tissue to be a single compartment with instantaneous exchange of the labeled spins from the vessels, and

Buxton's model, more complex models have been proposed that include the effects of label dispersion. However, none has been established as suitable for routine use for the analysis of ASL data [71].

Therefore in this work, to obtain an approximate estimation of the perfusion values, the mean CBF value over the gray matter was calculated using the following formula, derived from the General kinetic model:

$$\Delta M = 2M_0 . \frac{f}{\lambda} . T_{1g} \alpha e^{\frac{-\Delta t}{T_{1g}}} \qquad \textbf{4.1}$$

where ΔM is the perfusion weighted image, M_0 the reference scan, f the CBF we want to calculate, λ the blood/brain coefficient of water, T_{1g} the T_1 in GM, which is assumed to be equal to blood T_1, α the inversion efficiency and Δt the post labeling delay.

Chapter 5

Methods

5.1 General Considerations

All four studies were conducted in a similar approach, starting with the recruitment of participants, followed by a set of experimental measurements and subsequent analysis of the images obtained. Specifications of each study are described later in this Chapter.

5.1.1 Volunteer Recruitment

A total of twenty three healthy volunteers with ages between 18 and 55 years old were recruited from the staff of the Max Plank Institute for Biological Cybernetics and an online database (https://experiments.tuebingen.mpg.de/). After obtaining written informed consent from the subjects, they were included in the experimental measurements performed between June 2014 and November 2014.

5.1.2 Selection of the Labeling Plane and Imaging Region

The labeling plane was selected in reference to the Anterior-Commissure Posterior-Commissure (AC-PC) line, approximately between 74 and 94 mm below the line (see **Figure 5.1**), since quantitative analysis revealed that the averaged signal intensity is highest when the label plane is positioned at 84 mm below the AC-PC line [72] .

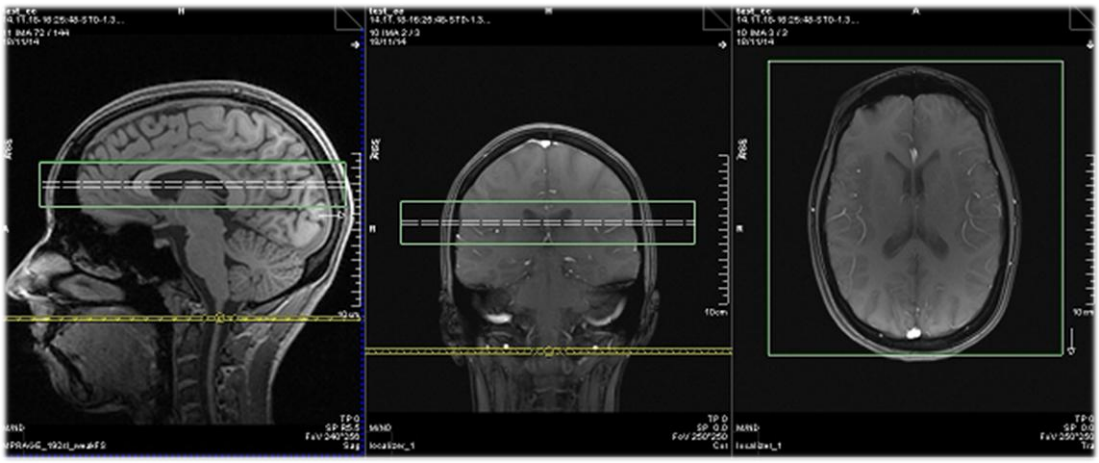

Figure 5.1 – Positioning of the tag **(yellow)** and slice region **(green)**.

5.1.3 Experimental Measurements

Perfusion images were acquired on a Siemens Magnetom Prisma (Siemens Medical Solutions, Erlangen, Germany) with a magnetic field strength of 3T using a 20 channel head/neck coil (Siemens).

Each session protocol consisted of a brain localizer with TR/TE=8.6/4.0 ms, flip angle=20°, Field of view (FOV)=230×256 mm2 and approximate duration of 20 s, followed by a high resolution T_1 weighted anatomical scan MPRAGE (Magnetization Prepared Rapid Gradient Echo) with TR/TE=17.5 ms/2.8 ms, flip angle=90°, FOV=256×240 mm2, matrix size=180×192, 144 slices, slice thickness=1.3 mm and duration 5 min.

The anatomical scan was followed by several perfusion measurements where the pCASL sequence and/or parameters were varied, according to the study in question. All pCASL scans were performed in a randomized manner and using strong fat suppression to avoid chemical shift artifacts.

In an initial experiment, preceding the ones presented in this dissertation, these artifacts were evident. We started by using fat saturation to suppress the fat signal. However, even using fat saturation, these artifacts appeared in the last slices acquired, due to fast T_1 relaxation of the fat signal. Therefore to overcome this issue, we opted for the application of a saturation pulse before each slice acquisition.

5.1.4 Data Analysis

We implemented a simple post-processing routine that could be applied to the studies conducted. Data was processed offline using SPM8 (Wellcome Department of Imaging Neuroscience, London, UK) and self-written software in MATLAB R2011a (Mathworks, Natick, MA). PCASL data was converted to DICOM format, motion corrected, co-registered and segmented using SPM8. A self-written program was used to calculate the difference between control and label images (pairwise subtraction). The first two pairs were discarded and the others were segmented using the gray matter mask obtained previously in SPM. Then, the difference images were averaged, in order to obtain a perfusion weighted image.

5.1.4 .1 Motion Correction

Taking into account that subject motion is one of the main sources of noise in ASL, trying to minimize the error induced by the motion is fundamental. To accomplish that, motion correction was performed using the realignment function in SPM. The purpose of realignment is to align all images, so that the positioning of the brain in each image is the same. In each series of measurements, tag and control images were aligned to the first control image. We also considered realigning all tag images to the first tag image and all control images to the first control. However, independent realignment of label and control images had been implemented before and the results weren´t significantly different from regular realignment [73].

Motion correction in SPM8 is performed using a rigid body transformation, meaning that the size of the brain is kept constant. First, the parameters needed to apply the transformation are determined using the image selected as reference. There are a total of 6 parameters, three rotations (over the x, y, and z-axis), and three translations (left-right, up-down, and forward-backward), which fully describe the movement of the head over time. After estimating the values of those parameters the transformation is applied to the remaining images.

In addition, the software from Siemens automatically returned not only the tag and control images, but also a series of images already realigned, called MOCO series [74]. We

decided to use the dataset were we compared flip angles and bandwidths of the inversion pulses to evaluate the performance of both motion correction methods.

5.1.4 .2 Co-registration and Segmentation

After realignment, the tag and control images were aligned with the anatomical image, so that, after subtraction and averaging, perfusion is superimposed onto the correct anatomical location. The procedure described previously is named co-registration. The last step performed in SPM consisted in segmenting the brain into three maps of gray matter, white matter and CSF, respectively, using the co-registered T_1 volume. Each image obtained is, in fact, a probability map and to avoid signal contributions from unwanted tissues, we applied a threshold to the GM map, where only pixels with a probability of belonging to GM superior to fifty percent were included. The threshold value was established based on observations. The mask was applied to isolate GM in the brain and also remove the background signal.

5.1.5 SNR Calculation and CBF Estimation

SNR is typically used as a quantitative measure of image quality and provides a direct means for comparison of signal obtained with different imaging methods. The temporal SNR (tSNR) of the perfusion images was calculated as the mean perfusion image divided by the standard deviation across the difference images (control – tag). It was then averaged over the entire gray matter, to obtain the mean gray matter SNR value. In addition, the spatial SNR (sSNR) was also calculated as the mean gray matter value of the perfusion weighted image divided by the standard deviation of an image region outside of the brain.

For an approximate estimation of quantitative perfusion values, the CBF was estimated using the formula **4.1** (see section 4.5). Given that the slices are not acquired instantaneously, we measured the time between each slice acquisition to correct the post labeling delay for each slice, in order to obtain a more accurate CBF quantification. In **Table 5.1**, the values of the static parameters used for CBF estimation are presented.

Table 5.1 – Values used for CBF quantification.

Parameter	Corresponding value
α	0.94
λ	0.9
Δt (ms)	1800 (1300 for pCASL-TrueFISP)
T_{1g} (ms)	1330

5.1.6 Statistical Analysis

After obtaining the mean tSNR for each slice, for each subject and each sequence, those values were exported to Excel (Microsoft Office Excel 2007, Microsoft Corporation). The mean tSNR was obtained by averaging the tSNRs of all slices. The first and last slices were discarded, since the re-slicing step during realignment resulted in a considerable loss of signal in those slices. Differences between mean gray matter SNR measured with the sequence parameters were tested using One-way ANOVA tests or paired t-tests, depending on the study. Further analysis to determine not just whether there were any differences among the means, but specifically which pairs of means were significantly different was achieved using the MATLAB function *multcompare*, from the Statistics Toolbox, that accounts for errors associated to multiple comparisons, therefore, avoiding false positives that could arise from performing multiple t-tests. Differences were regarded as significant if $p<0.05$ for all statistical tests performed.

5.2 Determination of the Optimal Bandwidth and Flip Angle of the Inversion Pulses

The bandwidth of an RF pulse describes the frequency range of the pulse. Very few ASL studies report the bandwidth of the inversion pulses used [75]. So far, for pCASL the impact of different bandwidths in the inversion efficiency and SNR hasn´t been addressed at clinical field strength. Lowering the pulse bandwidth will decrease the thickness of the labeling plane. On the other hand, high transmitter bandwidth can lead to problems with SAR due to the higher RF amplitude necessary.

Therefore, we decided to evaluate the impact of different bandwidths on the SNR of the perfusion images. With that purpose, three pCASL sequences were tested, each having inversion pulses with different bandwidths (see **Figure 5.2**). The bandwidth of the inversion pulses was determined by the FT of the pulses shapes represented bellow. For each inversion pulse, the bandwidth results were the following, 2262 Hz for the Gauss pulse, 2662 Hz for the F768 and 3222 Hz for the FDA.

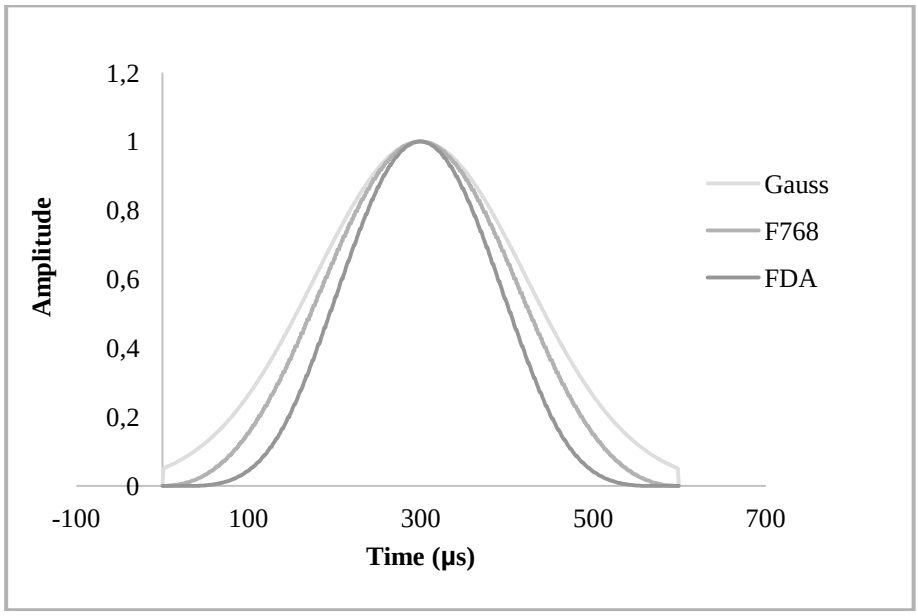

Figure 5.2 – Inversion pulse shapes used for pCASL labeling. The horizontal axis represents the temporal domain. Since frequency has an inverse relation with time, Gauss pulse has the smallest bandwidth of the tree pulses represented, while FDA has the highest bandwidth.

In addition, within the same experiment, we also investigated the influence of the inversion pulse's flip angle on the SNR. For each inversion pulse shape, measurements were done with three different flip angles (20, 24, 28 degrees), since previous studies reported the optimal flip angle to be in the range of 20° to 30° for pCASL [48].

5.2.1 Data Acquisition

Six volunteers, four males and two females with ages between 18 and 40 years participated in the study. The scan began with a brain localizer to choose the labeling plane

and slice location. In addition, a high resolution T_1 weighted image was acquired. The parameters used in these acquisitions were the same as presented in section 5.1.3.

Imaging parameters for pCASL sequences with single-shot gradient echo EPI as readout were the following: labeling duration=1500 ms, post labeling delay=1800 ms , number of controls/labels=56 pairs, RF duration=0.6 ms, pause between RF pulses=0.6 ms, TR=4000 ms, FOV=240×240, matrix size=64×64, voxel size=3×3 mm, bandwidth=2.7 kHz, 12 slices acquired in ascending order, slice thickness=3 mm, distance factor between slices=20, TE= 21 ms, and scan duration 8 min.

A total of 9 runs were performed varying the pulse shape and flip angle. That is, each sequence (Gauss, FDA, F768) was measured thrice with different flip angles.

5.3 Implementation of Background Suppression with Different Degrees of Suppression

If the static tissue signal varies between image acquisitions, either because of motion, frequency changes or machine instability, the subtraction images will be corrupted. Attenuation or suppression of the background noise in ASL can greatly improve sensitivity and reproducibility [62].

For pCASL, background suppression was achieved using two pre-saturation pulses before labeling, selective to the imaging region, and two additional inversion pulses, timed in order to null the background tissue signal at time of readout (see **Figure 5.3**). The first inversion pulse was applied right after the labeling and the second 1487 ms after the first.

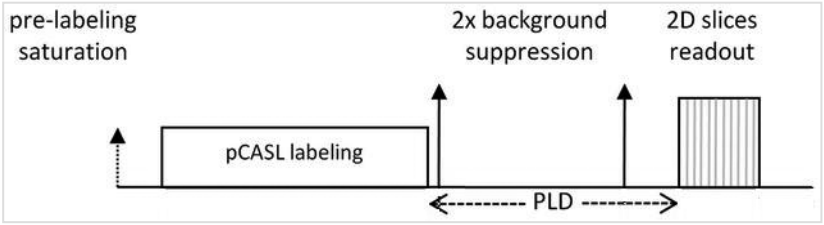

Figure 5.3 – PCASL timing diagram with background suppression pulses.

Additionally, different degrees of suppression were applied, by changing the timing of the second inversion pulse. Since perfect background suppression causes complications in

post-processing and prohibits motion correction, the BS efficiency was reduced by shifting the maximum suppression in five steps from 0 ms to 500 ms forward.

5.3.1 Data Acquisition

Six volunteers, 3 males and 3 females with ages between 18 and 55 years participated in the study. In the selection of the acquisition parameters, the results from the previous study about inversion pulse bandwidth and flip angle were taken into account.

Imaging parameters for all pCASL runs were identical: Gauss inversion pulses, labeling duration=1500 ms, post labeling delay=1800 ms, FA=28°, number of controls/labels=56 pairs, RF duration=0.6 ms, pause between RF pulses=0.6 ms, single-shot gradient echo EPI as readout, TR=4000 ms, FOV=240×240, matrix size=64×64, voxel size=3×3 mm, bandwidth=2.7 kHz, 8 slices acquired in ascending order, slice thickness=3 mm, distance factor between slices=20, TE= 21 ms, and scan duration 8 min.

5.3.2 Data Post-processing

In an initial attempt, magnitude images were used and data analysis was performed as described in section 5.1.4. However, for pCASL with background suppression, magnitude reconstruction can lead to perfusion errors, since the additional inversion pulses flip the magnetization and, at the time of readout, label and control may have different signal [73]. In order to account for these circumstances, all BS image data were also saved as complex raw data and reconstructed offline with custom-made software. The processing steps were the same, but using complex values instead.

5.4 Comparison of Balanced and Unbalanced pCASL and Readout Sequences EPI and TrueFISP

Concerning the readout scheme, EPI is a commonly used method for ASL, but it suffers from distortion artifacts and TrueFISP has been suggested as an alternative readout that overcomes these limitations, while maintaining relatively high temporal resolution and SNR [1]. PCASL sequences have been implemented in two different ways concerning the

labeling gradient moment, balanced and unbalanced pCASL. The results obtained with the two schemes provide comparable performance in general, though unbalanced pCASL is expected to be less sensitive to off-resonance effects at the labeling plane [48].

In this study, three variations of the pCASL sequence were tested, balanced and unbalanced pCASL, both with EPI readout and balanced pCASL with TrueFISP readout.

5.4.1 Data Acquisition

Six volunteers, 3 males and 3 females with ages between 18 and 55 years participated in the study.

Imaging parameters for balanced and unbalanced pCASL-EPI experiments were: Gauss inversion pulses, labeling duration=1500 ms, post labeling delay=1800 ms, FA=28°, number of controls/labels= 56 pairs, RF duration=0.6 ms, pause between RF pulses=0.6 ms, single-shot gradient echo EPI, TR=4000 ms, FOV=240×240, matrix size=64×64, voxel size=3×3 mm, bandwidth=2.7 kHz, 8 slices acquired in ascending order, slice thickness=3 mm, distance factor between slices=20, TE=21 ms, and scan duration 8 min.

For balanced pCASL with TrueFISP readout the bandwidth and tag delay were reduced to 0.98 KHz and 1300 ms, respectively, in order to reduce the acquisition time. Also, TR and TE were adjusted to 3.16 ms and 1.58 ms and we used 5/8 partial Fourier encoding.

5.5 Evaluation of the Quality of Perfusion Images Obtained with Two Different Head Coils

RF-Coils are used to generate the varying magnetic field for spin excitation or to receive the MR signal [76].

In the previous studies, we used a 20 channel head coil for signal reception. In this experiment, we decided to measure perfusion with the same sequence, balanced pCASL, and same parameters, with another head coil (64 channel head coil) and compare the SNRs obtained. Since image quality is expected to increase with the number of channels, the anticipated result would be an increase in SNR when using the 64 channel head coils, instead of the regular 20 channel head coil.

5.5.1 Data Acquisition

Five volunteers with ages between 18 and 40 years participated in the study. This experiment was divided in two parts, since the subject had to be removed from the scanner in order to replace the 20 channel head coil for the 64 channel coil and repeat the measurements. The first part of the experiment was realized with the 20 channel head coil. The anatomical scan was followed by a perfusion measurement with the balanced pCASL sequence. A total of 123 images were acquired, of which the first image corresponds to the reference scan. The parameters of the acquisition were the following: single-shot gradient echo EPI, FOV=240×240, matrix size=64×64, voxel size=3×3 mm, 8 slices acquired in ascending order, slice thickness=3 mm, distance factor between slices=20, labeling duration=1500 ms, post labeling delay=1800 ms, TR=4000 ms, TE=21 ms, number of controls/labels=61 pairs, RF duration=0.6 ms, pause between RF pulses=0.6 ms, labeling pulse flip angle=28°, bandwidth=2.7 kHz, and scan duration 8 min.

After this procedure the subject was removed from the scanner and the coil was replaced by the 64 channel coil. We repeated all the previous measurements. Slice positioning was done manually, in approximately the same region of the brain as the one chosen for the first part of the experiment.

Chapter 6

Results

6.1 Optimal bandwidth and Flip Angle of the Inversion Pulses

Subsequent to the processing steps in SPM, tag images were subtracted from control images and averaged, producing a perfusion weighted image. The tSNR for each slice was determined as mean perfusion image divided by the standard deviation of the single perfusion images, across the temporal series and then averaged over the entire gray matter. Resulting tSNRs images from one of the subject measured can be found in **Figure 6.1** prior to averaging over the gray matter.

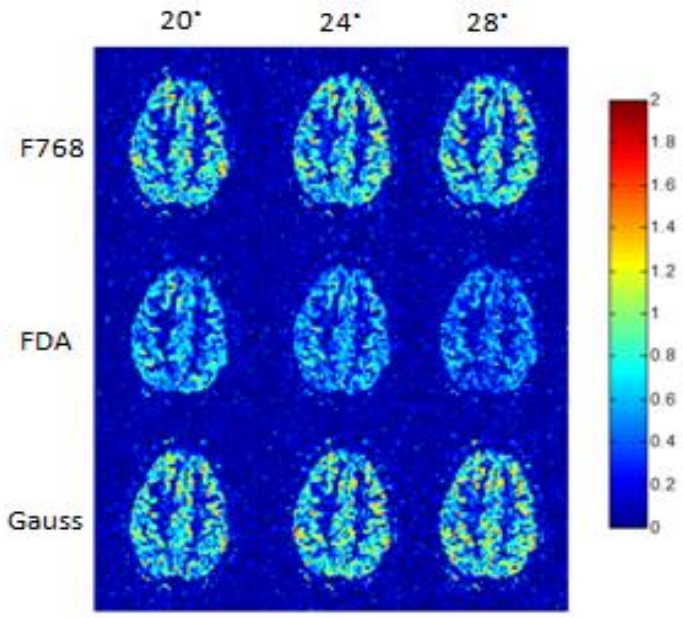

Figure 6.1 – tSNR images of the first slice for different pulse shapes and flip angles from one of the subjects measured. The flip angle is represented in the columns and the pulse shape in the rows.

Based solely on the results from this single individual we observe that, regardless of the flip angle, the tSNR obtained with the pulse FDA is clearly inferior to the ones achieved with the other two pulses (see **Figure 6.1**). This outcome was also noticeable in the images obtained from the other subjects measured. Further analysis was necessary in

order to objectively compare the image quality associated with the different pulse shapes and flip angles.

For this study, the results of the two firsts and lasts slices were discarded due to loss of signal caused by re-slicing, in the motion correction step. Therefore, we obtained a total of forty eight measurements of gray matter tSNR for each pair pulse shape/flip angle, since we measured six subjects and for each, we computed the values of eight slices. Those values were averaged and the results are shown in **Figure 6.2** with corresponding standard deviations.

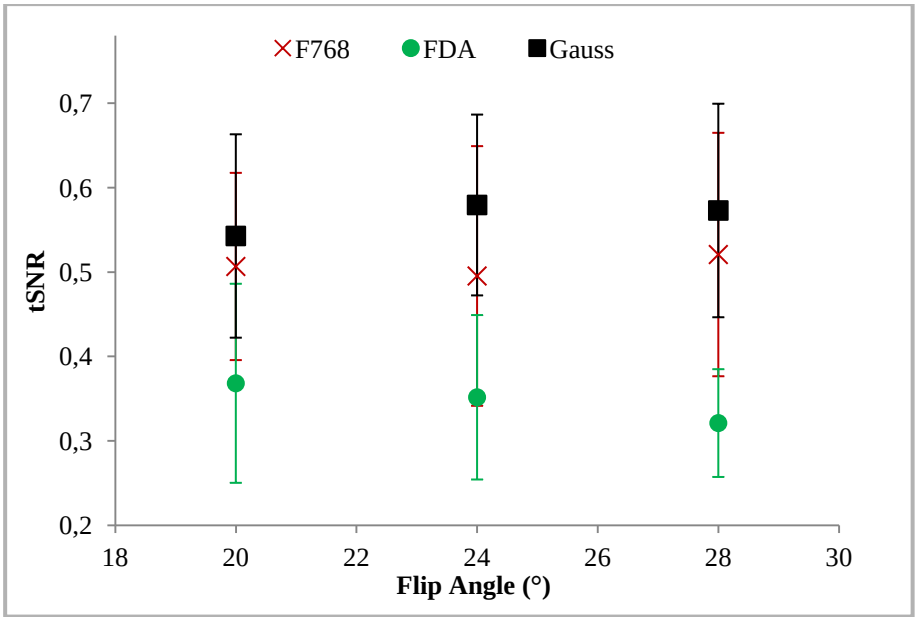

Figure 6.2 – Mean gray matter tSNR and corresponding standard deviation for varied pulse shapes and flip angles.

After averaging the results, the inferences from **Figure 6.1**, concerning the low performance of the pulse FDA were confirmed. These pulses yield, on average, the smallest tSNR for each flip angle. On the other hand, Gauss pulses showed a tendency to provide the best image quality. However, for the flip angles 20° and 28° the tSNR achieved with the pulse shape F768 had similar results as the Gauss pulse. The influence of the flip angle was not clear, since each pulse shape attained the highest average tSNR with a different flip angle.

Besides the tSNR, we also obtained CFB images. All evaluated sequences generated good perfusion images where gray matter structures could be differentiated. Typical results of perfusion from a volunteer using Gauss pulse shape and 24° flip angle are shown in **Figure 6.3**.

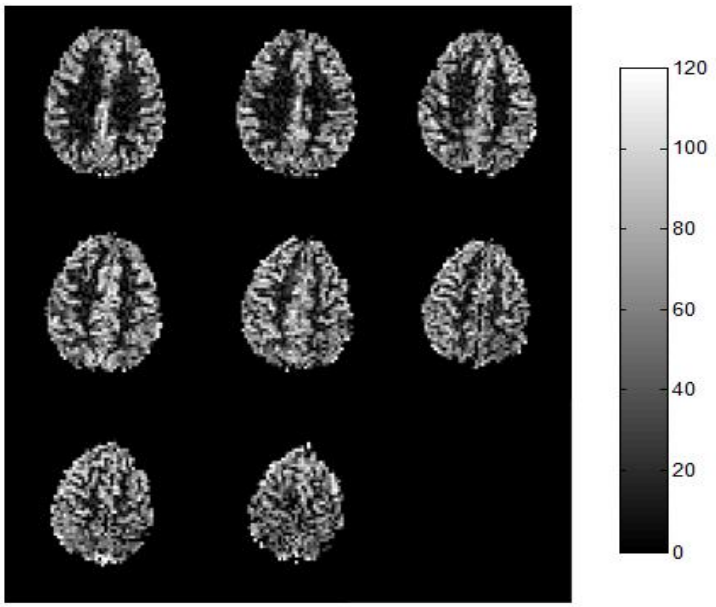

Figure 6.3 – CBF maps for gauss pulse shape and flip angle equal to 24°.

CBF values were averaged over the entire gray matter. For that, we used the inversion efficiency values from simulations [16]. The quantification results are presented in **Table 6.1** as well as the tSNR values.

Table 6.1 – Mean gray matter tSNR and CBF for the different pulse shapes and flip angles tested.

Inversion Pulse	Flip Angle (°)	tSNR	CBF (ml/100g/min)
F768	20	0.46 ± 0.11	50.10 ± 6.84
	24	0.45 ± 0.15	49.86 ± 10.18
	28	0.47 ± 0.14	49.32 ± 10.14
FDA	20	0.32 ± 0.11	37.24 ± 6.80
	24	0.30 ± 0.09	34.53 ± 7.59
	28	0.27 ± 0.07	30.32 ± 7.40
Gauss	20	0.49 ± 0.12	50.15 ± 7.04
	24	0.53 ± 0.11	55.21 ± 6.56
	28	0.52 ± 0.13	57.20 ± 7.09

Concerning the tSNR, the highest value obtained was 0.53 ± 0.11 for an inversion pulse with Gauss shape and flip angle equal to 24º (see **Table 6.1**). However, this result was closely followed by the one obtained for the same pulse, but with flip angle equal to 28º.

Like the SNR, the highest CBF values were obtained for the Gauss pulse, whereas the lowest were achieved with FDA pulse. Observing the FDA results for the different flip angles, we notice a similar behavior between tSNR and CBF, meaning an increase in tSNR is followed by an increase in CBF.

A One-way ANOVA test was performed with the tSNR values of all subjects obtained for the different sequences. Results showed there were at least two sequences with significantly different mean tSNR, since $p = 2.92 \times 10^{-42}$. Further analysis to determine not just whether there are any differences among the means, but specifically which pairs of means are significantly different was necessary. We used the MATLAB function *multcompare*, from the Statistics Toolbox, that accounts for errors associated to multiple comparisons, therefore avoiding false positives that could arrive from performing multiple t-tests. For this test, each pair inversion pulse shape/flip angle was considered as a different group, whose means were compared (see **Figure 6.4**).

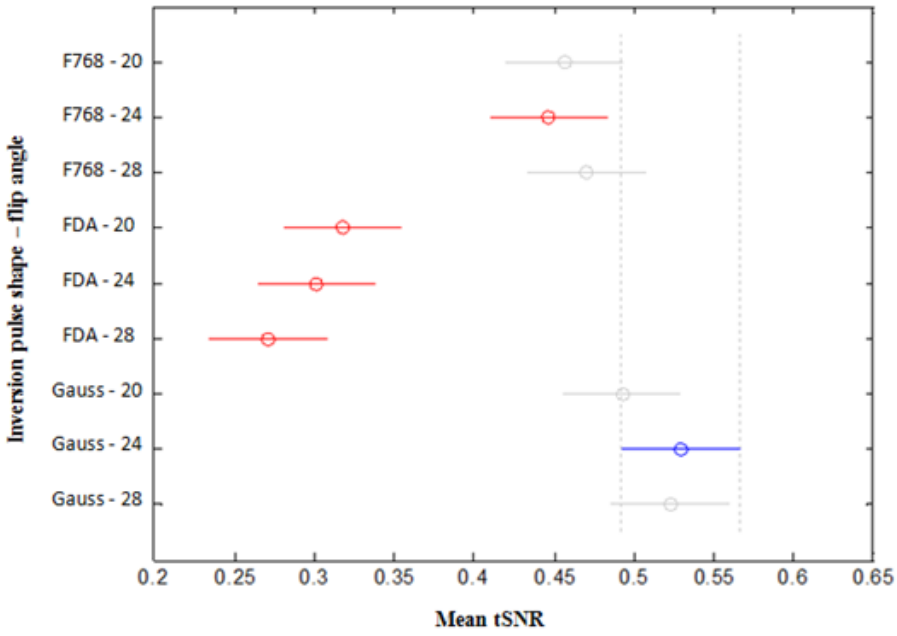

Figure 6.4 – *Multcompare* test results between groups tested. The blue dataset represents the selected group and in red the groups which possess a significantly different mean from the selected group. In this particular graphic, the selected group is Gauss-24 and there are four groups with means significantly different from that group, all FDA groups and F768-24.

A summary of the *multicompare* test results is presented below in **Table 6.2**.

Table 6.2 – Results from the statistical analysis between sequences. Only significant results are displayed below. In the second column, the sequences that have an average SNR significantly different from the corresponding sequence in the first column are presented.

Pulse shape – Flip Angle (°)	**Pulse shape – Flip Angle (°)**
FDA – all flip angles	Gauss / F768 – all flip angles
F768 – 20	FDA – all flip angles
F768 – 24	FDA – all flip angles / Gauss – 24 and 28
F768 – 28	FDA – all flip angles
Gauss – 20	FDA – all flip angles
Gauss – 24	FDA – all flip angles / F768 – 24
Gauss – 28	FDA – all flip angles / F768 – 24

As mentioned above, Gauss-24 possessed on average the highest SNR. Nevertheless, that result was not significantly different from Gauss-20, Gauss-28, F768-20 and F768-28.

On the other hand, FDA results were the lowest and significantly different from F768 and Gauss for all flip angles.

6.1.1 Comparison of SPM and Siemens Motion Correction

The scanner software contains a motion correction routine that automatically generates corrected images for all pCASL experiments. These images were processed similarly to the original images, with exception of the motion correction step, which was skipped in SPM. The values of the tSNR obtained with SPM motion correction and Siemens are presented in **Figure 6.5** for a comparative analysis. For the different runs, the tSNR obtained with the Siemens' motion correction routine is higher than the one obtained with SPM.

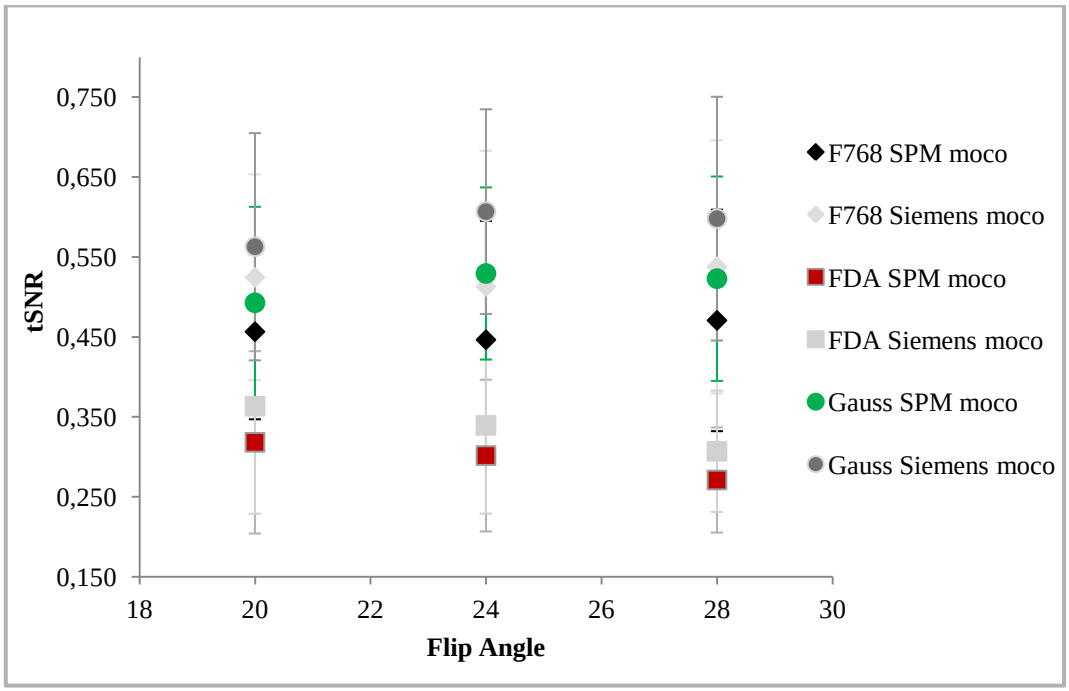

Figure 6.5 – Graphical representation of the tSNR for each pulse shape and flip angle for Siemens and SPM motion corrections.

With the purpose of evaluating if the increase in SNR was significant between the Siemens and SPM motion correction routines, we performed a statistical analysis. For that, paired t-tests were carried out for each run between SPM and Siemens motion correction and the values can be seen in **Table 6.3**.

Table 6.3 – Paired t-test results between SNR obtained with SPM and Siemens motion correction for each sequence and flip angle.

Pulse Shape - Flip angle (°)	p values	Significant
F768 - 20	1.4×10^{-24}	Yes
F768 - 24	1.6×10^{-21}	Yes
F768 - 28	7.9×10^{-24}	Yes
FDA - 20	7.1×10^{-19}	Yes
FDA - 24	1.8×10^{-15}	Yes
FDA - 28	1.6×10^{-26}	Yes
Gauss - 20	2.2×10^{-24}	Yes
Gauss - 24	1.5×10^{-26}	Yes
Gauss - 28	8.1×10^{-24}	Yes

Observing **Table 6.3**, we notice that for all the sequences and flip angles the tSNR values obtained with the two motion corrections were significantly different. Hence, the tSNR achieved with Siemens motion correction were higher than the ones obtained using SPM motion correction, suggesting a better performance of Siemens' routine for motion correction. However, it is necessary to consider the algorithms used in each implementation.

6.2 Background Suppression with Different Degrees of Efficiency

6.2.1. Magnitude Reconstruction Results

Since background suppression can reduce noise from motion and other sources of instability, performing motion correction for suppressed data might not be necessary. We investigated the influence of doing/not doing motion correction in the tSNR, for different BS efficiencies.

It is extremely relevant to take into account that magnitude reconstruction, for a near perfect BS, results in incorrect estimation of perfusion, because tag and control images may have different signs resulting in negative or zero perfusion values (see **Figure 6.6**). That is the reason why in **Table 6.4** and **6.5** the tSNR is so low for d=0 and d=100. However, for the time being we are only interested in looking at the variation of signal between the two tables and not at the values themselves.

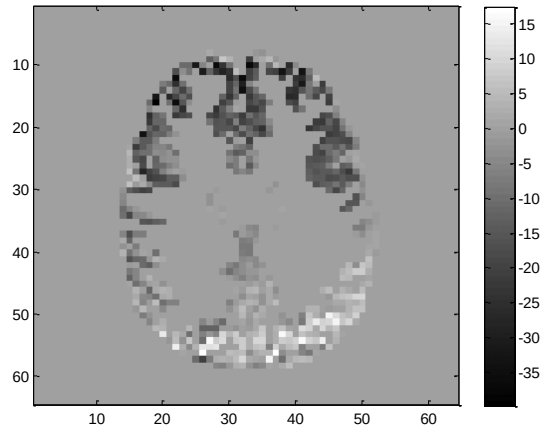

Figure 6.6 – Perfusion weighted image obtained with magnitude reconstructed data for complete background suppression. Negative perfusion values were obtained due to changes in the polarity of the background signal.

In section 6.2.2, results of complex subtraction of tag and control data are displayed. Complex analysis allowed maximizing the degree of suppression without compromising the results. Therefore in that section, the outcome of a comparative analysis between the tSNRs obtained for different BS efficiencies is presented.

With magnitude reconstructed data, we investigated the need of performing motion correction for background suppressed data. We performed the post-processing routine described in section 5.1.4 and repeated it again for the same data, but skipping the realignment step. Results from both analyses can be seen below, in **Table 6.4** with and in **Table 6.5** without motion correction.

Table 6.4 – SNR values obtained for different values of maximum suppression shift (d). One data set without suppression was also acquired. These results were obtained for data that was motion corrected using SPM.

d (ms)	Subject 1	Subject 2	Subject 3	Subject 4	Subject 5	Subject 6	tSNR	SD
0	0.34	0.18	0.24	0.52	0.35	0.23	**0.31**	**0.12**
100	0.78	0.34	0.45	0.45	0.63	0.15	**0.47**	**0.21**
200	1.18	0.68	0.71	0.85	0.97	0.81	**0.87**	**0.18**
300	1.30	0.72	0.81	1.22	1.08	1.08	**1.03**	**0.22**
400	1.23	0.67	0.88	1.12	1.04	0.60	**0.92**	**0.25**
500	1.29	0.73	0.78	1.11	1.09	0.82	**0.97**	**0.22**
Without Suppression	0.75	0.37	0.52	0.73	0.62	0.70	**0.62**	**0.14**

Table 6.5 – SNR values obtained for different values of maximum suppression shift (d). Also one data set without suppression was acquired. These results were obtained for data that was not motion corrected.

d (ms)	Subject 1	Subject 2	Subject 3	Subject 4	Subject 5	Subject 6	tSNR	SD
0	0.45	0.39	0.27	0.43	0.45	0.39	**0.40**	**0.06**
100	0.79	0.58	0.48	0.62	0.77	0.76	**0.67**	**0.12**
200	1.05	0.87	0.64	0.88	0.93	1.03	**0.90**	**0.14**
300	1.08	0.73	0.65	1.01	1.01	1.02	**0.92**	**0.17**
400	1.05	0.62	0.70	0.94	0.99	1.00	**0.88**	**0.17**
500	1.03	0.67	0.66	0.92	1.01	1.04	**0.89**	**0.18**
Without Suppression	0.72	0.28	0.45	0.68	0.61	0.62	**0.56**	**0.16**

From **Tables 6.4** and **6.5** the results indicate that for a stronger suppression (smaller d values) performing motion correction leads to a decrease in the SNR. The causes of this decrease were investigated and a possible explanation is presented below (see **Figure 6.7**). For d>200, motion correction can be performed correctly and leads to an increase in the SNR.

With the aim of identifying the cause of the decrease in SNR for SPM motion correction data with attenuation of the static tissue, we looked at the estimated head motion correction parameter time course in the z direction from one dataset with background suppression, where the shifting from the maximum suppression was zero, meaning a near perfect suppression of the static tissue signal (see **Figure 6.7**).

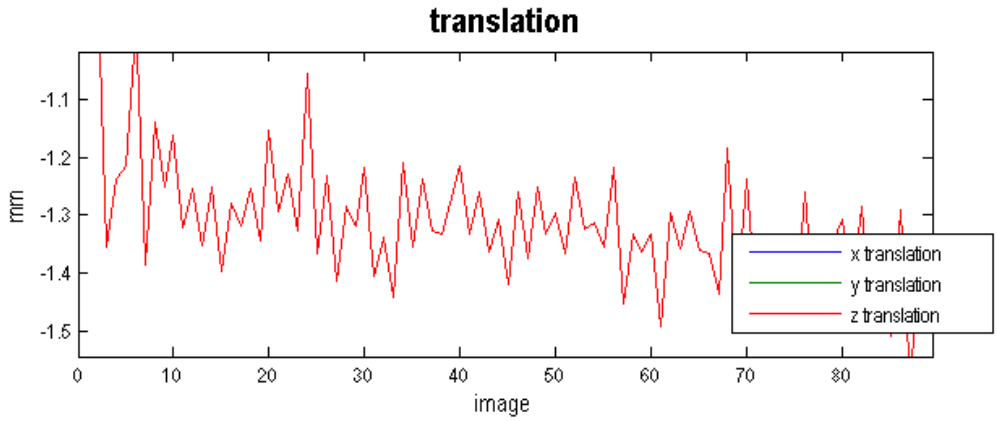

Figure 6.7 – Estimated head motions along z direction obtained in SPM for pCASL background suppressed data (d=0).

The spurious motion estimation observed above has been reported, for motion correction procedures that use a six parameter rigid body realignment routine, to be prominent in imaging sequences such as pCASL with BS, in which the effect of image label is large with respect to the overall image intensity. In these situations, motion correction routines can interpret the perfusion effect as a systematic displacement of head position between the label and control images [73].

Furthermore, identical results were obtained for the other translations as well as rotations (data not shown). This spurious motion correction estimation was becoming less noticeable in datasets with increasing values of shifting from the maximum suppression.

6.2.2 Complex Reconstruction Results

For analysis of complex data, all post-processing steps were performed using exclusively self-written MATLAB scripts. No motion correction was performed and therefore we could include all eight slices acquired in the calculations. The mask to segment GM was obtained from the measurement without suppression with magnitude reconstruction, acquired from the analysis in the previous section. In addition, we used an in-house MATLAB routine that allowed redefining the mask and correcting it manually.

Good results were achieved since it was possible to differentiate GM structures from the others tissues in the perfusion weighted images (see **Figure 6.8**). Also, we succeeded in implementing different degrees of attenuation of the static tissue, with the signal from control images following the expected pattern, almost inexistent signal for optimal suppression and a small increase in signal as the image acquisition is shifted with respect to the time of optimal suppression.

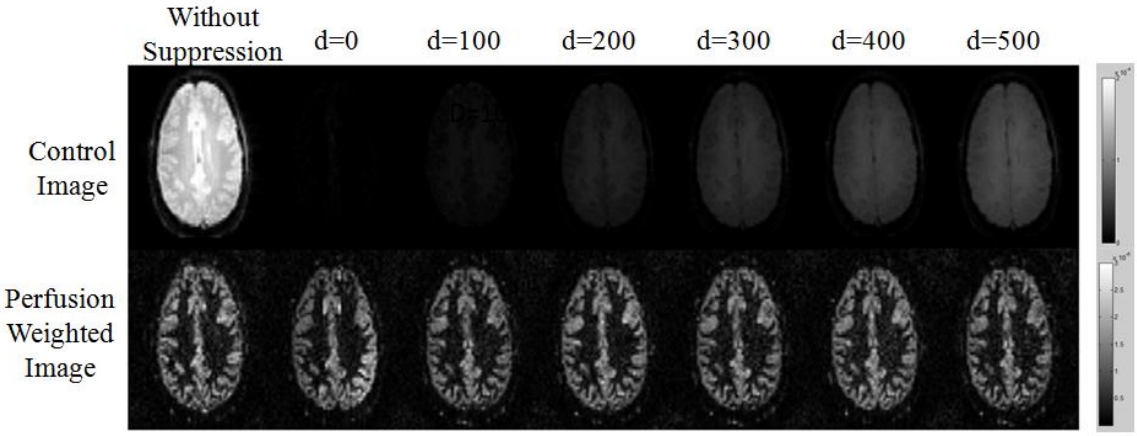

Figure 6.8 – Representation of the control **(top)** and perfusion weighted images **(bottom)** for different intensities of background suppression for the same slice and subject.

The remaining unsuppressed signal was calculated for all shifts (d) as the mean suppressed signal divided by the mean unsuppressed signal (obtained from the data set without suppression) of control images. Our purpose was to check how the shifting in steps of 100 ms was influencing the degree of suppression. Theoretically, d=0 ms corresponds to the optimal background suppression, however the experimental results show that, for the mentioned value, there was still 15% of signal left to suppress. In addition, for d=100 there was slightly less remaining unsuppressed signal than for d=0, but the differences were not significant (see **Figure 6.9**). The remaining unsuppressed signal increases with the shifting time, showing that we were able to accomplish perfusion measurement using different efficiencies of suppression.

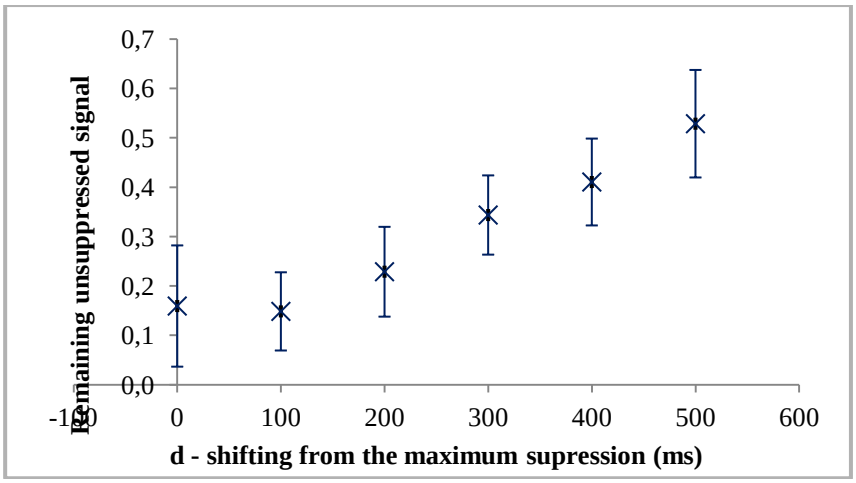

Figure 6.9 – Graphical representation of the remaining unsuppressed signal for different values of shift from the maximum suppression.

For d=0 and d=100, a considerable degree of suppression was achieved, causing a reduction in image intensity to about 16% and 15% of the original background signal, respectively. This considerable degree of suppression resulted in increased tSNR of the perfusion series when compared to other datasets, where attenuation of the static tissue signal was not as strong (see **Figure 6.10**).

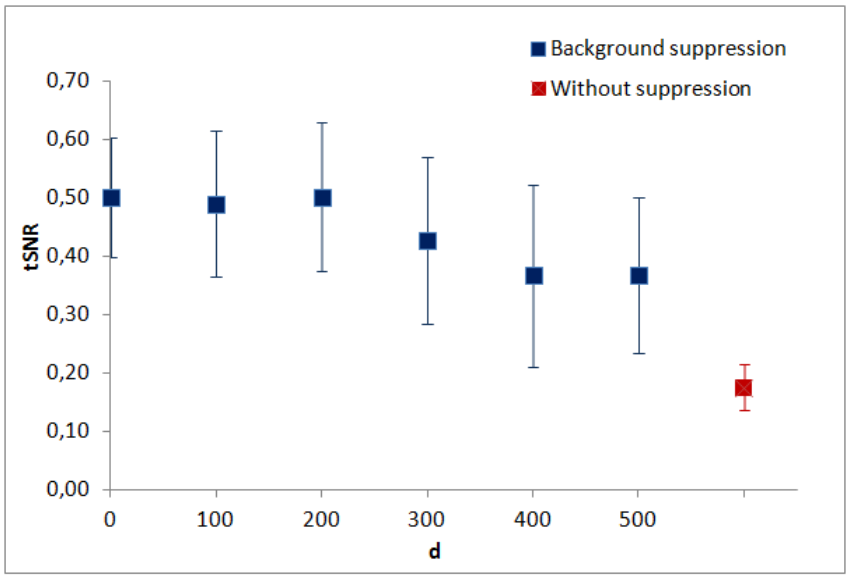

Figure 6.10 – Representation of the tSNR for different degrees of suppression applied by varying the parameter d (shifting from the maximum suppression). A dataset without suppression was also acquired.

The images without background suppression possessed in average the lowest tSNR. For suppressed data, the highest tSNR values were achieved with d between 0 and 200. For d>200 there was a decrease in tSNR when increasing the value of d. In order to verify if there was a relationship between tSNR and the remaining unsuppressed signal, we plotted the two variables (see **Figure 6.11**). The correlation value obtained was $R^2 \cong 0.97$, confirming the existence of a inverse relation with linear proportion between the two variables. In other words by decreasing the remaining unsuppressed signal it is possible to increase the SNR.

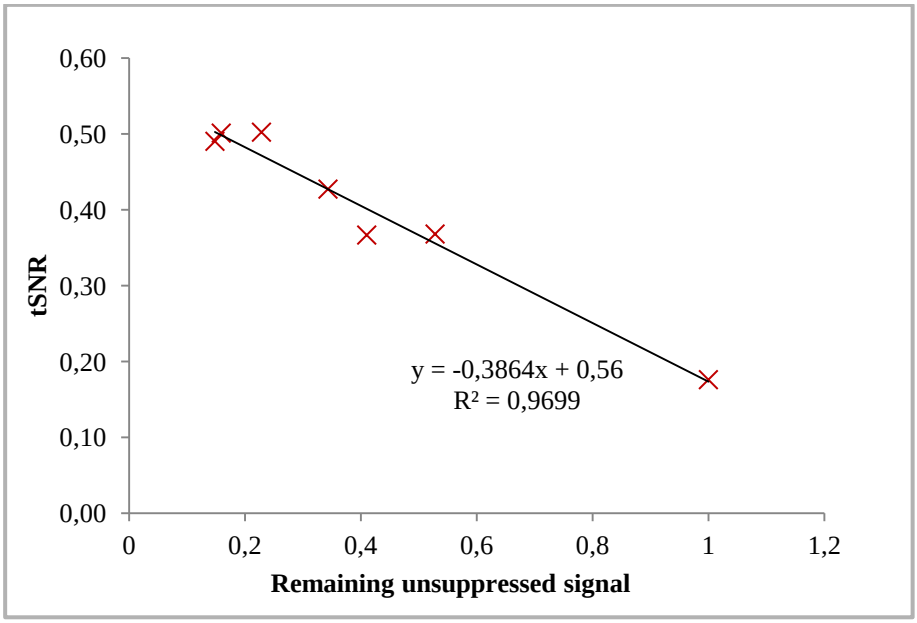

Figure 6.11 – Graphical representation of tSNR in function of remaining unsuppressed signal. Correlation value indicates a linear relation between the two variables.

In order to verify if the changes in the degree of suppression had a significant influence in the tSNR, we performed a One-way ANOVA test for two different groups. First, we used all datasets including the one without suppression, resulting in a value of $p = 1.98 \times 10^{-30}$, indicating the existence of significant differences between the means of the groups. Based on the data shown in **Figure 6.10**, the tSNR of the data without suppression is clearly the one that differs mostly from the others. Therefore, we repeated the test using only suppressed datasets. Again, the result, $p = 5.89 \times 10^{-11}$, showed that there were at least two datasets with significantly different mean tSNRs. So, with the purpose of finding which groups had different means, a multi-comparison test was done.

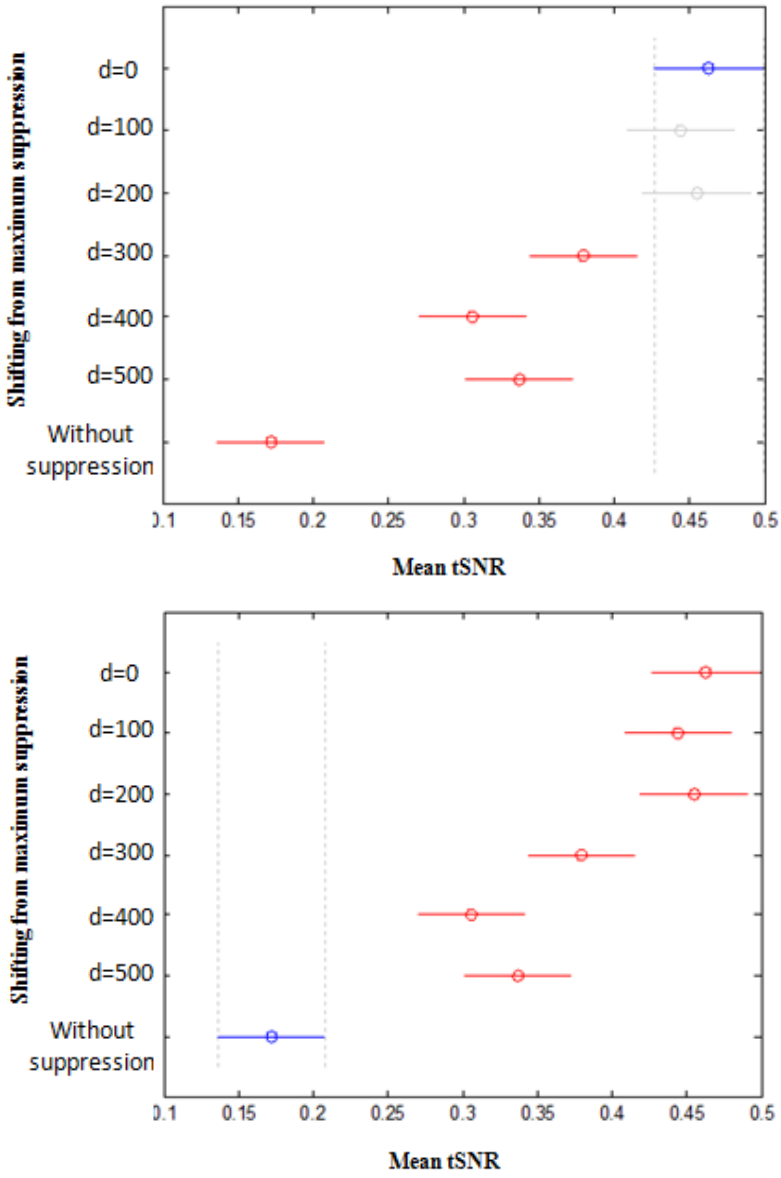

Figure 6.12 – *Multcompare* test results between groups. The selected group is shown in blue and in red the groups which possess a significantly different mean from the selected group. On top, the selected group is d=0 and there are four groups with means significantly different from that group, d=300, d=400, d=500, and without suppression. Below, the selected group is without suppression and all other groups have means significantly different from that group.

From the analysis of **Figure 6.10** and **Figure 6.12** we notice that varying the time of the second inversion pulse up to 200 ms from the optimal value found in simulations has no significant impact on the tSNR of the perfusion images. Additionally, the data set without suppression had a significantly lower tSNR than all the other groups.

6.3 Balanced/Unbalanced pCASL and EPI/ TrueFISP Readout

Using the procedures described in the methods, we calculated the tSNR of the perfusion images. The results for balanced and unbalanced pCASL with EPI readout are similar, even though the unbalanced had in average a higher tSNR (see **Figure 6.13**). Regarding balanced pCASL-TrueFISP, its tSNR was superior to the ones achieved with the other sequences.

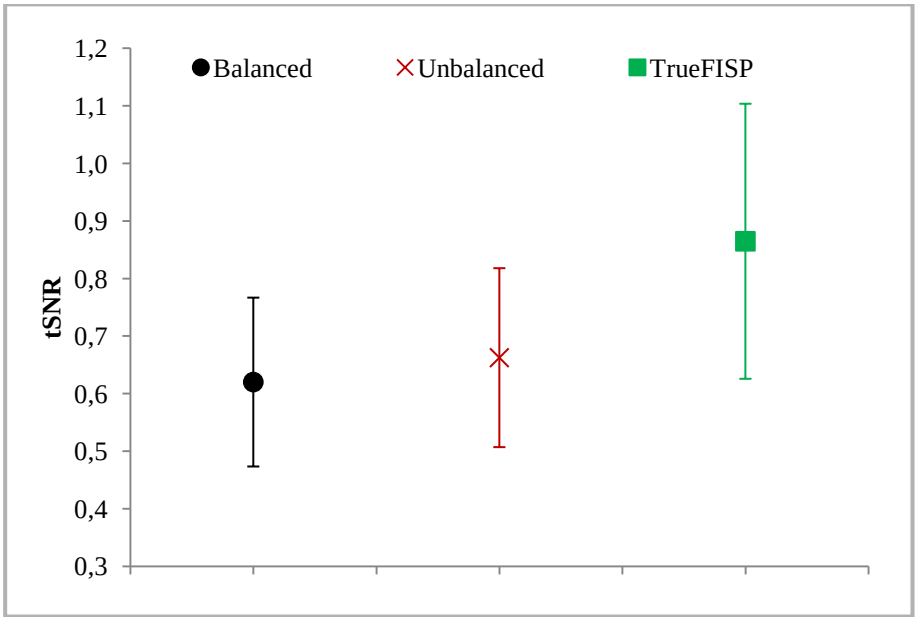

Figure 6.13 – Graphical representation of the tSNR obtained for the three sequences tested, balanced pCASL with EPI readout **(black)**, unbalanced pCASL with EPI readout **(red)** and balanced pCASL with TrueFISP readout **(green)**.

We estimated CFB values and averaged them for each sequence. Exemplar images of gray matter CBF are presented in **Figure 6.14**. The average values are displayed in **Table 6.6** along with the tSNR values for each sequence.

Figure 6.14 – Gray matter CBF image for balanced pCASL-EPI **(left)**, unbalanced pCASL-EPI **(middle)** and balanced pCASL-TrueFISP **(right)**, for the fifth slice from one of the subjects measured.

Table 6.6 – Mean gray matter tSNR and CBF for the different sequences tested.

Sequence	tSNR	CBF
Balanced EPI	0.62 ± 0.14	59.15 ± 7.72
Unbalanced EPI	0.66 ± 0.14	58.58 ± 5.77
Balanced TrueFISP	0.86 ± 0.29	56.69 ± 6.95

The highest SNR was achieved for the TrueFISP sequence for a value of $\text{tSNR} = 0.86 \pm 0.29$. To compare TrueFISP readout with EPI, that is, the influence of the readout scheme, we can only look at balanced EPI and TrueFISP data, since the unbalanced method has a slightly different labeling sequence. TrueFISP provides in average a higher tSNR when compared to EPI. However, it also has a higher variation across subjects that can be perceived through the error bars in **Figure 6.13**.

Concerning the sequences with EPI readout, regardless of the gradient moment of tag and control acquisitions, i.e. the labeling sequence being balanced or unbalanced, the tSNR results were identical, 0.62 ± 0.14 and 0.66 ± 0.14, respectively. This outcome is in agreement with previous studies, which reported comparable performance between results obtained with the two schemes [4].

In order to evaluate the statistical significance of the results in **Table 6.6**, we performed a One-way ANOVA test to compare the mean SNR values of the three sequences. The result, $p = 2.87 \times 10^{-6}$, indicates a significant difference in the means of at least two groups. Additionally, a multi comparison test was performed (see **Figure 6.15**)

with the purpose of finding out specifically which sequences had significantly different values of tSNR.

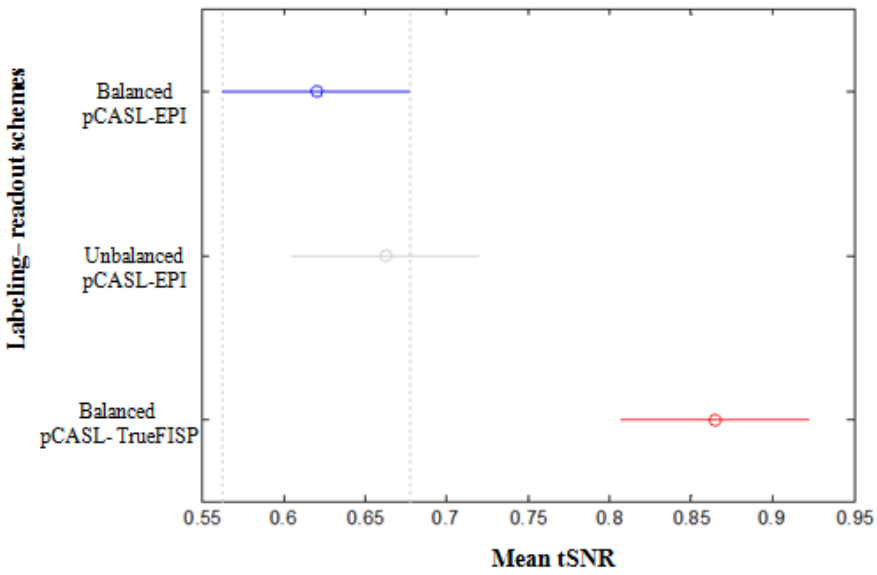

Figure 6.15 – *Multcompare* test results between groups tested. In blue is represented the group selected and in red the groups which possess a significantly different mean from the selected group.

The statistical test outcome showed that the means of balanced pCASL-EPI and unbalanced pCASL-EPI are not significantly different. Though, their means are significantly different from the mean of balanced pCASL-TrueFISP sequence.

Table 6.7 – Gray matter tSNR for pCASL-TrueFISP per slice for each subject measured. The average tSNR decreases per slice.

TrueFISP SNR	Slice 2	Slice 3	Slice 4	Slice 5	Slice 6	Slice 7
Subject 1	1.50	1.34	1.35	1.11	0.96	0.83
Subject 2	0.66	0.64	0.62	0.44	0.41	0.38
Subject 3	0.96	0.78	0.71	0.67	0.51	0.40
Subject 4	1.34	1.27	1.13	0.98	0.86	0.69
Subject 5	1.06	1.02	0.92	0.83	0.73	0.51
Subject 6	1.13	1.04	0.89	0.83	0.77	0.67
Average tSNR per slice	**1.11**	**1.02**	**0.94**	**0.82**	**0.71**	**0.58**

Results above (see **Table 6.7**) strongly evince a decrease in SNR per slice. EPI results also decreased per slice, although, the loss of signal was much smaller. For EPI,

since each slice is acquired with only one excitation pulse, it causes signal dropout with time and consequently the last slices have less signal.

6.4 Coils Experiment

In this study, we measured perfusion on the same subjects and with the same sequence, balanced pCASL with EPI readout, using two different head coils with 20 and 64 channels. The average tSNR obtained with each coil was assessed.

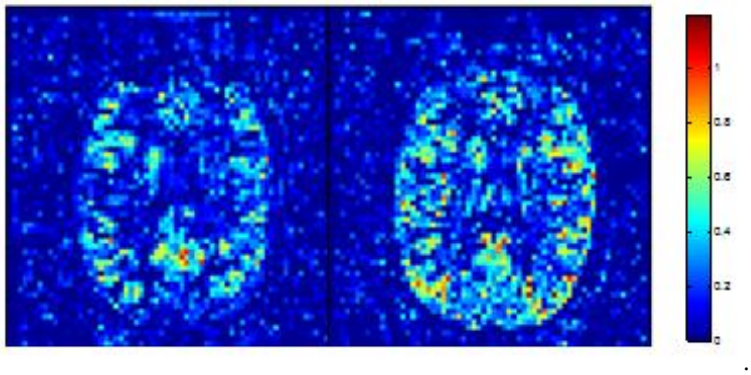

Figure 6.16 – tSNR images for the subject 3 acquired with the 20 channel head coil **(left)** and the 64 channel head coil **(right).**

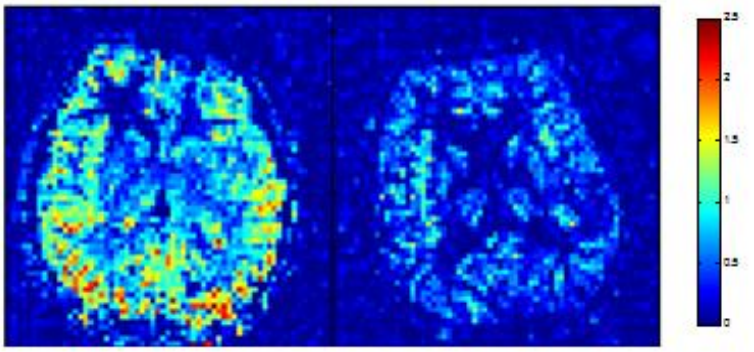

Figure 6.17 – tSNR images for the subject 5 acquired with the 20 channel head coil **(left)** and the 64 channel head coil **(right)**.

Observing **Figures 6.16** and **6.17** we notice that the two subjects had completely different results. The perfusion images of subject 3 acquired with the 64 channel head coil have a higher tSNR than the images obtained with the 20 channel coil. However, subject 5 (see **Figure 6.17**) has the opposite result, having in average for the 20 channel

measurements an tSNR much higher than any previously obtained tSNR value for the same sequence and coil (see **Table 6.1** for Gauss-28°).

Table 6.8 – Average Gray matter tSNR of the perfusion images obtained with the 20 and 64 channel head coil for each subject.

tSNR of the perfusion weighted images		
Subject	**20 channel head coil**	**64 channel head coil**
1	0.51	0.48
2	0.47	0.35
3	0.19	0.31
4	0.50	0.36
5	0.93	0.29
Average	0.52 ± 0.26	0.36 ± 0.07

After averaging the results obtained for the five subjects measured, the images obtained with the 20 channel head coil had an average tSNR higher than the ones obtained with the other coil. Aiming to ascertain if the mean tSNR attained for both coils were different, we did a paired t-test, obtaining a p value equal to 0.001, implying the means are significantly different. Since these results were not expected, we examined the tSNR of the control images.

Table 6.9 – Average Gray matter tSNR of the control images obtained with the 20 and 64 channel head coil.

tSNR of the control images		
Subject	**20 channel head coil**	**64 channel head coil**
1	80.78	69.66
2	71.98	124.56
3	34.16	65.35
4	105.27	123.76
5	32.67	51.02
Average	64.97 ± 31.29	86.87 ± 34.73

Considering that for control images the tSNR is higher for the measurements performed with the 64 channel head coil, except for one subject, we excluded the possibility of the previous results (see **Table 6.9**) being due to technical aspects of the coil or scanner.

Chapter 7

Discussion

The major aim of this project was the experimental optimization of a pCASL sequence. Since the sequence possesses a great variety of parameters that could be enhanced, either in the labeling or the readout component, we decided to focus on the following variables: inversion pulse shape and flip angle, both tested in the same study, implementation of background suppression with different degrees of efficiency, comparison of the balanced and unbalanced labeling strategies and EPI and TrueFISP readout. Finally, we measured perfusion using different coils. By varying the parameters mentioned above we investigated their influence on the tSNR and CBF to determine which setting, among to the parameters tested, could provide the best image quality.

7.1 Optimal Flip Angle and Bandwidth of the Inversion Pulses

7.1.1 tSNR

Concerning the first study, whose aim was to compare the performance of three different inversion pulse shapes with different bandwidths (Gauss, F768 and FDA) and three flip angles (20, 24 and 28 degrees), the results were not conclusive regarding the choice of an optimal bandwidth and flip angle. None of the parameters stood out as the best approach with significant results from the other sequences tested. On the other hand, FDA pulses had an average tSNR significantly inferior to Gauss and F768 pulses, for each flip angle, having therefore the worst performance. We concluded that higher inversion pulse bandwidth is not desirable since it leads to a decrease in SNR, when compared to results obtained with smaller bandwidths. Additionally, the decrease in tSNR is most likely caused by a decrease in inversion efficiency, suggesting that increased pulse bandwidth reduces the inversion efficiency.

In view of the fact that the Gauss pulse shows a tendency to yield a higher tSNR than F768 regardless of the flip angle, we selected it as the recommended implementation for the following studies. Moreover, for Gaussian pulses, the variations of the flip angle didn´t

significantly affect the tSNR, therefore the choice of the best flip angle was based on the tendency shown by Gauss-24° to yield in average the highest tSNR and the fact that Gauss-28° had almost the same mean value as Gauss-24°. The difference between both results was in the order of a decimal. Even though we could not find an optimal flip angle value, the choice of 24° or 28° provided images with the highest tSNR, assuring a good image quality. Furthermore, the flip angle dependence is in accordance with previous studies [16, 77].

7.1.2 CBF

In this initial study, the pCASL sequences hadn´t yet incorporated the acquisition of a reference scan (M_0), hence the use of the first control image as the reference image for CBF estimation. Ideally, the inversion efficiency should have been measured for each pair pulse shape/flip angle, using phase-contrast velocity mapping [72]. However, that was not possible due to time constraints.

The CBF results obtained with F768 and Gauss pulses are in the range of what is considered normal (40-100 mL/min/100 g) [11]. However, that wasn´t true for FDA average CBF values, whose range doesn´t intercept the values mentioned above. While much effort was put in the choice of a gray matter mask threshold that would allow selecting only gray matter voxels, the relatively low CBF values obtained for all sequences could be explained by partial volume effects caused by residual white matter signal. Additionally, the use of a control image as reference might have also contributed to the low perfusion values.

7.1.3 Motion Correction Strategies

Despite many proposed corrections and compensation strategies, motion remains one of the most significant problems in ASL examinations [78]. In our work, we compared two motion correction techniques. Both of them make use of the most common strategy for handling motion artifacts, that is, retrospective motion correction [79]. These post-processing approaches use a variety of algorithmic, iterative approaches applied in the

image domain as well as in k-space. The motion correction routine implemented by SPM estimates motion in six directions (3 translations and 3 rotations), while the Siemens' routine only does a 2D correction, meaning that it only shifts the images within their slices.

Utilizing Siemens' motion corrected data we can obtain perfusion images with a higher tSNR than when performing motion correction using SPM realignment, as demonstrated by the results in **Figure 6.5**.

Additionally, the results of a separate experiment, prior to the optimization tests, where one subject was scanned with the pCASL sequence, showed also a better performance from Siemens' motion correction technique. Perfusion was measured twice, in the first run we told the subject to avoid head movement, as usual. However in the second run, we specifically asked the subject to move his head during measurements. Results for the second run can be observed in Annex A. These findings suggest that Siemens' technique can perform better than SPM for large motion. That could be explained by the fact that SPM successfully corrects for small amounts of motion, 1-3 mm in any direction, but if a subject moved more than 6 mm in any direction in the course of the entire experiment, motion artifacts may be expected in the results [80].

Even though Siemens motion correction provided images with a higher tSNR, the SPM routine may be more suitable for ASL, since it accounts for motion in all directions, whether Siemens only performs an in-plane correction. As such, disregarding motion along certain orientations can result in perfusion quantification errors, since CBF is derived from signal changes between label and control conditions and is therefore highly sensitive to head motion, especially between the control and the label image within each pair.

7.2 Background Suppression for pCASL

We accomplished the goal established for this study, to be precise, the implementation of background suppression with different degrees of suppression. Even though we did not achieve perfect suppression of the static tissue signal, a reduction of up to 85% of the signal is a considerable amount, which had a significant impact on the tSNR of the perfusion images.

Performing BS, even only with partial attenuation, can result in better image quality than using no suppression technique at all. We showed that by shifting the maximum of the

suppression by 200 ms forward, it is possible to use magnitude data for perfusion calculation and to perform motion correction while still having an increased tSNR. However, ideally, complete background suppression is the optimal choice, for which complex reconstruction has to be performed to avoid errors in perfusion.

In 2D multislice strategies, like EPI single shot readout, BS can be optimal for one slice, but is progressively less efficient for other slices. In fact, it was possible to observe a small increase in signal from slice to slice (see Annex B). However, even if not completely effective, performing background suppression was still beneficial since it had a significant impact on the tSNR. Furthermore, our results demonstrate the existence of an inverse relationship with linear proportion between remaining unsuppressed signal and the tSNR. In other words, the more efficient the suppression, the lower the remaining unsuppressed signal and consequently higher tSNRs are achieved.

Results are in agreement with other studies that show an improvement in image quality when using background suppression [11, 62].

7.3 Gradient Moment of pCASL and Readout Sequences

No significant differences were observed in the tSNR obtained with balanced and unbalanced pCASL with EPI readout, suggesting that the gradient moment of the labeling scheme did not affect image quality. However, the slightly lower tSNR of the balanced sequence might be caused by off-resonance effects at the labeling plane.

As to the readout sequence, TrueFISP readout yielded a better tSNR, being significantly higher than the EPI's average value. However, it also had a large variability not only across subjects but even between slices in the same subject. In fact, the decrease in SNR per slice observed for TrueFISP readout is most likely caused by T_1 relaxation due to the long acquisition time, since each slice requires more than one excitation to be imaged. TrueFISP is sensitive to off-resonance, and can be sensitive to flow related artifacts which might be the cause of the variability [81].

Even though EPI is usually the most common readout method for 2D acquisitions, it suffers from distortion artifacts (see section 4.4) and TrueFISP has been suggested as an alternative readout that overcomes these limitations while maintaining relatively high temporal resolution and SNR [68]. Our results are in accordance with the previous

affirmation, however, TrueFISP is not suitable for large multislice acquisitions due to signal drop caused by T_1 relaxation and by an increase in acquisition time.

Concerning the CBF values, all sequences obtained reasonable values, though TrueFISP's value was the lowest due to the decrease in tag delay during acquisition.

7.4 Coil Influence in the tSNR

In contrast to expectations, the higher tSNR was achieved with the 20 channel head coil. Considering that both coils were used repeatedly, with the 64 channel coil achieving higher tSNRs in several experiments, we eliminated from the start the hypothesis of a bad coil design or malfunction.

There are, however, several factors to take into account. First, in order to trace the source of the problem, we calculated the tSNR of control images, the same way we did for the perfusion weighted image. The tSNR obtained from control images was higher for the 64 channel head coil for all subjects. Therefore, the expected results were found for control images. The procedure was repeated for tag images as well and the outcome was the same. This way, we deleted the hypothesis of the results being caused by technical imperfections or human errors during acquisition.

Additionally we also calculated the sSNR of the perfusion images. The values obtained followed the same pattern as the tSNR. Up to this point the most probable cause of the results would be some alteration in perfusion.

We considered the fact that all subjects were measured after performing an fMRI study for another project that involved looking at a visual stimulus. And in order to avoid taking the patient out several times, we always measured perfusion first with the 20 channel coil, since it was the one used in the fMRI study. Looking at subject 5 (see **Figure 6.17**) it is clear there is an increase in tSNR in the posterior brain. These results were also noticeable for subject 3 and 4, even though less evident. However, the possibility of a residual increase in perfusion due to the stimulus from the previous study is not coherent, since Subject 3 had normal results. We also deliberated if the fact that the subjects had to move to switch the coil could have enhanced their perfusion. This thought was contradicted by the results; in fact most subjects had higher perfusion values during the

first measurement. The variations in perfusion between subjects require further investigation to establish the cause of the inconsistent results.

Chapter 8

Conclusions

This project was developed for the purpose of optimizing a pCASL sequence for ASL studies, with the aid of experimental tests. The experimental protocol allowed evaluating the impact of parameters such as inversion pulse bandwidth and flip angle, background suppression, labeling gradient moment, readout sequence and the number of channels of a coil, on the tSNR of the perfusion images and also on CBF.

All sequences implemented were able to measure perfusion and a good contrast between gray and white matter was achieved. The resulting analysis suggested that a higher inversion pulse bandwidth is not desirable, since the inversion efficiency seems to decrease with increasing pulse bandwidth. Additionally, Gauss pulses with a flip angle equal to 24° provided the best outcome. The flip angle dependence is in accordance with previous studies [16]. As expected, data measured with background suppression yielded a significantly higher tSNR. Performing only partial suppression, by shifting the time of optimal suppression by up to 200 ms, allows motion correction without significant loss in SNR and does not require complex reconstruction, simplifying the post-processing steps. As to the labeling gradient moment, balanced and unbalanced sequences achieved a comparable performance without significant differences.

Concerning the readout scheme, even though TrueFISP's SNR values were higher than EPI values, the increase in acquisition time limited the number of slices possible in a given repetition time. Therefore, EPI remains the first choice as a readout scheme for pCASL. Regarding the coils, the perfusion results were not clear, but it was shown, for control images, that an increased number of channels provides better image quality.

Summarizing, our main contribution consisted in the development of a reliable sequence well suited for future experimental investigations of cerebral perfusion. The parameters we recommend, based on the experimental results, are the use of a Gaussian inversion pulse with a flip angle equal to 24º or 28º and background suppression to maximize the tSNR of the resulting images and provide a more accurate CBF quantification. The readout should be selected according to the purpose of the study, however, for multislice studies, EPI is preferable to TrueFISP.

Chapter 9

Future Work

The pCASL sequence has a complex structure, comprising several components. In this study we aimed to optimize that particular sequence, however, we only tested a small variety of parameters that could be optimized. Therefore, numerous aspects could be further investigated in future research, regarding not only the sequence itself but also the quantification of CBF.

One possible implementation, that was not part of this project, would be to perform perfusion measurements using unbalanced pCASL with background suppression, given that this method is less sensitive to off-resonance effects than the balanced version. Alternatively, we could apply multi-phase pCASL to reduce sensitivity of the CBF estimation to phase mismatches caused by magnetic field inhomogeneities (off-resonance) on the inversion plane [82]. Additionally, an accurate CBF quantification could be performed, using different post labeling delays to calculate arterial transit time and also measuring the inversion efficiency in-vivo.

Another pertinent feature that should be tested is the ability of the sequence to detect perfusion changes. In order to accomplish that, fMRI ASL studies could be performed, for instance, using a visual stimulus with block design consisting of alternated periods of rest and activation. As a result, in the subsequent analysis, it should be possible to detect an increase in perfusion in the visual cortex during activation.

Having obtained dubious results for the coil experiment, the procedures should be repeated, this time in a larger sample, varying the order of the measurements and without performing any kind of study before that could induce perfusion changes.

Finally, it would be interesting to assess the sequences' performance in another scanner with similar field strength, in order to test their reliability.

References

[1] P. Tofts, *Quantitative MRI of the Brain: Measuring Changes Caused by Disease*. John Wiley & Sons, 2005, p. 650.

[2] A. R. Deibler, J. M. Pollock, R. A. Kraft, H. Tan, J. H. Burdette, and J. A. Maldjian, "Arterial Spin-Labeling in routine clinical practice, part 1: technique and artifacts," *American Journal of Neuroradiology*, vol. 29, no. 7, pp. 1228–34, 2008.

[3] D. C. Alsop and J. A. Detre, "Multisection cerebral blood flow MR imaging with continuous arterial spin labeling," *Radiology*, vol. 208, no. 2, pp. 410–416, 1998.

[4] J. A. Detre, W. Zhang, D. A. Roberts, A. C. Silva, D. S. Williams, D. J. Grandis, A. P. Koretsky, and J. S. Leigh, "Tissue specific perfusion imaging using arterial spin labeling," *NMR in Biomedicine*, vol. 7, no. 1–2, pp. 75–82, 1994.

[5] D. S. Williams, J. A. Detre, J. S. Leigh, and A. P. Koretsky, "Magnetic resonance imaging of perfusion using spin inversion of arterial water," *Proceedings of the National Academy of Sciences of the United States of America*, vol. 89, no. 1, pp. 212–216, Jan. 1992.

[6] J. A. Detre, H. Rao, D. J. J. Wang, Y. F. Chen, and Z. Wang, "Applications of arterial spin labeled MRI in the brain," *Journal of Magnetic Resonance Imaging*, vol. 35, no. 5, pp. 1026–1037, 2012.

[7] S. Petcharunpaisan, J. Ramalho, and M. Castillo, "Arterial spin labeling in neuroimaging.," *World Journal of Radiology.*, vol. 2, no. 10, pp. 384–98, 2010.

[8] J. M. Pollock, H. Tan, R. A. Kraft, C. T. Whitlow, J. H. Burdette, and J. A. Maldjian, "Arterial Spin Labeled MRI Perfusion Imaging: Clinical Applications," *Magnetic Resonance Imaging Clinics of North America*, vol. 17, no. 2, pp. 315–338, 2009.

[9] P. B. Barker, X. Golay, and G. Zaharchuk, *Clinical Perfusion MRI: Techniques and Applications*. Cambridge University Press, 2013, p. 368.

[10] R. L. Wolf and J. A. Detre, "Clinical Neuroimaging Using Arterial Spin-Labeled Perfusion MRI," *Neurotherapeutics*, vol. 4, no. 3, pp. 346–359, 2007.

[11] D. C. Alsop, J. A. Detre, X. Golay, M. Günther, J. Hendrikse, L. Hernandez-Garcia, H. Lu, B. J. Macintosh, L. M. Parkes, M. Smits, M. J. P. van Osch, D. J. J. Wang, E. C. Wong, and G. Zaharchuk, "Recommended implementation of arterial spin-labeled perfusion MRI for clinical applications: A consensus of the ISMRM perfusion study group and the European consortium for ASL in dementia," *Magnetic Resonance in Medicine*, vol. 73, no. 1, pp. 102–116, 2015.

[12] J. A. Detre, J. S. Leigh, D. S. Williams, and A. P. Koretsky, “Perfusion imaging,” *Magnetic Resonance in Medicine*, vol. 23, no. 1, pp. 37–45, 1992.

[13] R. R. Edelman, B. Siewert, D. G. Darby, V. Thangaraj, A. C. Nobre, M. M. Mesulam, and S. Warach, “Qualitative mapping of cerebral blood flow and functional localization with echo-planar MR imaging and signal targeting with alternating radio frequency,” *Radiology*, vol. 192, no. 2, pp. 513–520, 1994.

[14] S. G. Kim, “Quantification of relative cerebral blood flow change by flow-sensitive alternating inversion recovery (FAIR) technique: application to functional mapping,” *Magnetic Resonance in Medicine*, vol. 34, no. 3, pp. 293–301, 1995.

[15] D. M. Garcia, C. Bazelaire, and D. C. Alsop, “Pseudo-continuous Flow Driven Adiabatic Inversion for Arterial Spin Labeling,” in *Proc. of 13th Meeting, International Society for Magnetic Resonance in Medicine, Miami , 2005*.

[16] R. Pohmann, J. Budde, E. J. Auerbach, G. Adriany, and K. Uğurbil, “Theoretical and experimental evaluation of continuous arterial spin labeling techniques,” *Magnetic Resonance in Medicine*, vol. 63, no. 2, pp. 438–446, 2010.

[17] A. Hendrix, “Magnets, Spins, and Resonances - An Introduction to the basics of Magnetic Resonance,” *Manuscript, Siemens Medical Solutions (Healthcare)*, 2003.[Online].Available:http://www.scmr.org/assets/files/members/documents/magnets_spins_resonances.pdf. [Accessed: 07-Dec-2014]

[18] Y. Gossuin, A. Hocq, P. Gillis, and Q. L. Vuong, “Physics of magnetic resonance imaging : from spin to pixel,” *Journal of Physics D: Applied Physics*, vol. 43, no. 21, pp. 1–41, 2010.

[19] R. Pohmann, “Physical Basics of NMR,” in *In vivo NMR Imaging, Methods in Molecular Biology*, vol. 771, no. 4, L. Schröder and C. Faber, Humana Press, 2011, pp. 3–21.

[20] P. Rinck, “The Basic Textbook of the European Magnetic Resonance Forum.” [Online]. Available: http://www.magnetic-resonance.org/ch/21-01.html. [Accessed: 17-Nov-2014].

[21] Y. Safriel, “MRI: Basic Principles and Applications,” *Yale Journal of Biology and Medicine*, vol. 76, no. 3, pp. 141–142, 2003.

[22] E. J. Blink, “MRI: Physics.” [Online]. Available: http://www.mri-physics.net. [Accessed: 13-Jan-2015].

[23] J. Petr, “Parallel Magnetic Resonance Imaging Reconstruction,” Czech Technical University, 2007.

[24] M. A. Brown and R. C. Semelka, *MRI: Basic Principles and Applications*. John Wiley & Sons, 2011, p. 280.

[25] M. J. Sands and A. Levitin, “Basics of magnetic resonance imaging,” *Seminars in Vascular Surgery*, vol. 17, no. 2, pp. 66–82, 2004.

[26] T. S. Curry III, J. E. Dowdey, and R. E. Murry Jr., *Christenseńs physics of diagnostic radiology*. Lippincott Williams & Wilkins, 1990, p. 522.

[27] D. G. Mitchell, D. L. Burk Jr, S. Vinitski, and M. D. Rifkin, “The biophysical basis of tissue contrast in extracranial MR imaging,” *American Journal of Roentgenology*, vol. 149, no. 4, pp. 831–837, 1987.

[28] “T1 and T2 relaxation diagram.”[Online].Available:http://www.vumc.com/branch/Children-White-Matter Disorders/419542/419673/745757/. [Accessed: 10-Dec-2014].

[29] J. P. Hornak, “The Basis of MRI.” [Online]. Available: https://www.cis.rit.edu/htbooks/mri/inside.htm. [Accessed: 05-Jan-2015].

[30] R. Pohmann, “Spatial Encodin - Basic Imaging Sequences,” in *In vivo NMR Imaging, Methods in Molecular Biology*, vol. 771, L. Schröder and C. Faber, Humana Press, 2011, pp. 23–43.

[31] A. Hendrix, “Magnets , Flows , and Artifacts,” *Manuscript, Siemens Med. Solut. (Healthcare)*, 2004. [Online]. Available: http://www.healthcare.siemens.com/siemens_hwem-hwem_ssxa_websites-context-root/wcm/idc/groups/public/@global/@imaging/@mri/documents/download/mdaw/mtqx/~edisp/magnets_flows_and_artifacts00016930.pdf. [Accessed: 10-Jan-2015].

[32] J. P. R. Sven Plein, John P. Greenwood, “Gradient Echo Versus Spin Echo,” in *Cardiovascular MR Manual*, Springer London, 2010, pp. 97–102.

[33] M. H. Pui and E. C. Fok, “MR imaging of the brain: comparison of gradient-echo and spin-echo pulse sequences,” *American Journal of Roentgenology*, vol. 165, no. 4, pp. 959–962, 1995.

[34] W. Rooney, “MRI: From Picture to Proton,” *Health Physics*, vol. 85. pp. 504–505, 2003.

[35] A. J. den Dekker and J. Sijbers, “Data distributions in magnetic resonance images: A review,” *Physica Medica: European Journal of Medical Physics*, vol. 30, no. 7, pp. 725–741, 2014.

[36] R. H. Hashemi, W. G. Bradley Jr, and C. J. Lisanti, *MRI: The Basics*. Lippincott Williams & Wilkins, 2012, p. 400.

[37] E. T. Petersen, I. Zimine, Y. C. L. Ho, and X. Golay, “Non-invasive measurement of perfusion: A critical review of arterial spin labelling techniques,” *The British Journal of Radiology*, vol. 79, no. 944, pp. 688–701, 2006.

[38] M. J. Donahue, M. K. Strother, and J. Hendrikse, “Novel MRI Approaches for Assessing Cerebral Hemodynamics in Ischemic Cerebrovascular Disease,” *Stroke*, vol. 43, no. 3, pp. 903–915, 2012.

[39] A. K. H. Miller, R. L. Alston, and J. A. N. Corsellis, “Variation with age in the volumes of grey and white matter in the cerebral hemispheres of man: measurements with an image analyser,” *Neuropathology and Applied Neurobiology*, vol. 6, no. 2, pp. 119–132, 1980.

[40] C. S. Yanofsky, “Understanding Multiple Sclerosis.” [Online]. Available: http://www.susqneuro.com/publications/ms/. [Accessed: 20-Jan-2015].

[41] G. Austin, D. Laffin, and W. Hayward, “Cerebral blood flow in patients undergoing microanastomosis for modification for prevention of stroke,” *Annals of Clinical and Laboratory Science*, vol. 5, no. 4, pp. 229–235, 1975.

[42] D. C. Alsop and J. A. Detre, “Reduced transit-time sensitivity in noninvasive magnetic resonance imaging of human cerebral blood flow,” *Journal of Cerebral Blood Flow & Metabolism*, vol. 16, no. 6, pp. 1236–1249, 1996.

[43] R. B. Buxton, L. R. Frank, E. C. Wong, B. Siewert, S. Warach, and R. R. Edelman, “A General Kinetic Model for Quantitative Perfusion Imaging with Arterial Spin Labeling,” *Magnetic Resonance in Medicine*, vol. 40, no. 3, pp. 383–396, 1998.

[44] X. Zhang, E. T. Petersen, E. Ghariq, J. B. De Vis, A. G. Webb, W. M. Teeuwisse, J. Hendrikse, and M. J. P. van Osch, “In vivo blood T(1) measurements at 1.5 T, 3 T, and 7 T,” *Magnetic Resonance in Medicine*, vol. 70, no. 4, pp. 1082–1086, 2013.

[45] H. Lu, C. Clingman, X. Golay, and P. C. Van Zijl, “Determining the longitudinal relaxation time (T1) of blood at 3.0 tesla,” *Magnetic Resonance in Medicine*, vol. 52, no. 3, pp. 679–682, 2004.

[46] E. T. Petersen, K. Mouridsen, and X. Golay, “The QUASAR reproducibility study, Part II: Results from a multi-center Arterial Spin Labeling test-retest study,” *Neuroimage*, vol. 49, pp. 104–113, 2010.

[47] “Labeling diagrams for ASL.” [Online]. Available: http://s434060124.online.de/aslindementiacms/basic-principles-of-asl-2. [Accessed: 12-Jan-2015].

[48] W. C. Wu, M. Fernández-Seara, J. A. Detre, F. W. Wehrli, and J. Wang, “A theoretical and experimental investigation of the tagging efficiency of pseudocontinuous arterial spin labeling,” *Magnetic Resonance in Medicine*, vol. 58, no. 5, pp. 1020–1027, 2007.

[49] W. Dai, D. Garcia, C. de Bazelaire, and D. C. Alsop, “Continuous flow-driven inversion for arterial spin labeling using pulsed radio frequency and gradient fields,” *Magnetic Resonance in Medicine*, vol. 60, no. 6, pp. 1488–97, 2008.

[50] K. K. Kwong, D. A. Chesler, R. M. Weisskoff, K. M. Donahue, T. L. Davis, L. Ostergaard, T. A. Campbell, and B. R. Rosen, “MR perfusion studies with T1-weighted echo planar imaging,” *Magnetic Resonance in Medicine*, vol. 34, no. 6, pp. 878–887, 1995.

[51] R. M. Henkelman, G. J. Stanisz, and S. J. Graham, “Magnetization transfer in MRI: a review,” *NMR in Biomedicine*, vol. 14, no. 2, pp. 57–64, 2001.

[52] J. A. Wells, “Arterial Spin Labelling Magnetic Resonance Imaging of the Brain : Techniques and Development,” University College London, 2010.

[53] W. T. Dixon, L. N. Du, D. D. Faul, M. Gado, and S. Rossnick, “Projection angiograms of blood labeled by adiabatic fast passage,” *Magnetic Resonance in Medicine*, vol. 3, no. 3, pp. 454–462, 1986.

[54] M. A. Bernstein, K. E. King, X. J. Zhou, and W. Fong, “Handbook of MRI Pulse Sequences,” Academic Press, 2004, p. 1040.

[55] P. Prasad, *Magnetic Resonance Imaging: Methods and Biologic Applications (Methods in Molecular Medicine)*. Humana Press, 2006, p. 447.

[56] J. Wang and D. J. Licht, “Pediatric perfusion MR imaging using arterial spin labeling,” *Neuroimaging Clinics of North America*, vol. 16, no. 1, pp. 149–167, 2006.

[57] M. Mezue, A. R. Segerdahl, T. W. Okell, M. A. Chappell, M. E. Kelly, and I. Tracey, “Optimization and reliability of multiple postlabeling delay pseudo-continuous arterial spin labeling during rest and stimulus-induced functional task activation,” *Journal of Cerebral Blood Flow & Metabolism*, vol. 34, no. 12, pp. 1919–1927, 2014.

[58] W. Dai, P. M. Robson, A. Shankaranarayanan, and D. C. Alsop, “Reduced resolution transit delay prescan for quantitative continuous arterial spin labeling perfusion imaging,” *Magnetic Resonance in Medicine*, vol. 67, no. 5, pp. 1252–1265, 2012.

[59] I. Asllani, A. Borogovac, and T. R. Brown, “Regression algorithm correcting for partial volume effects in arterial spin labeling MRI,” *Magnetic Resonance in Medicine*, vol. 60, no. 6, pp. 1362–1371, 2008.

[60] E. C. Wong, “Vessel encoded arterial spin labeling using pseudo-continuous tagging,” *Proc. of 14th Meeting, International Society for Magnetic Resonance in Medicine, Seattle*, 2006.

[61] W. T. Dixon, M. Sardashti, M. Castillo, and G. P. Stomp, “Multiple inversion recovery reduces static tissue signal in angiograms,” *Magnetic Resonance in Medicine*, vol. 18, no. 2, pp. 257–268, 1991.

[62] F. Q. Ye, J. A. Frank, D. R. Weinberger, and A. C. McLaughlin, “Noise reduction in 3D perfusion imaging by attenuating the static signal in arterial spin tagging (ASSIST),” *Magnetic Resonance in Medicine*, vol. 44, no. 1, pp. 92–100, 2000.

[63] D. M. Garcia, G. Duhamel, and D. C. Alsop, “Efficiency of inversion pulses for background suppressed arterial spin labeling,” *Magnetic Resonance in Medicine*, vol. 54, no. 2, pp. 366–372, 2005.

[64] N. Maleki, W. Dai, and D. C. Alsop, “Optimization of background suppression for arterial spin labeling perfusion imaging,” *Magnetic Resonance Materials in Physics, Biology and Medicine*, vol. 25, no. 2, pp. 127–133, 2012.

[65] J. Gregori, “Dynamic Arterial Spin Labeling Measurements of Physiological Parameters Permeability and Oxygenation,” Ruperto-Carola University of Heidelberg, 2009.

[66] M. Gunther, K. Oshio, and D. A. Feinberg, “Single-shot 3D imaging techniques improve arterial spin labeling perfusion measurements,” *Magnetic Resonance in Medicine*, vol. 54, no. 2, pp. 491–498, 2005.

[67] A. Boss, P. Martirosian, U. Klose, T. Nägele, C. D. Claussen, and F. Schick, “FAIR-TrueFISP imaging of cerebral perfusion in areas of high magnetic susceptibility differences at 1.5 and 3 Tesla,” *Journal of Magnetic Resonance Imaging*, vol. 25, no. 5, pp. 924–931, 2007.

[68] S. H. Park, D. J. J. Wang, and T. Q. Duong, “Balanced steady state free precession for arterial spin labeling MRI: Initial experience for blood flow mapping in human brain, retina, and kidney,” *Magnetic Resonance Imaging*, vol. 31, no. 7, pp. 1044–1050, 2013.

[69] P. Mansfield, “Multi-planar image formation using NMR spin echoes,” *Journal of Physics C: Solid State Physics*, vol. 10, no. 3, p. 55, 1977.

[70] A. Borogovac and I. Asllani, “Arterial Spin Labeling (ASL) fMRI: advantages, theoretical constraints, and experimental challenges in neurosciences,” *International Journal of Biomedical Imaging*, vol. 2012, p. 13, 2012.

[71] M. A. Chappell, M. W. Woolrich, S. Kazan, P. Jezzard, S. J. Payne, and B. J. MacIntosh, “Modeling dispersion in arterial spin labeling: validation using dynamic angiographic measurements,” *Magnetic Resonance in Medicine*, vol. 69, no. 2, pp. 563–570, 2011.

[72] S. Aslan, F. Xu, P. L. Wang, J. Uh, U. S. Yezhuvath, M. van Osch, and H. Lu, "Estimation of labeling efficiency in pseudo-Continuous Arterial Spin Labeling," *Magnetic Resonance in Medicine*, vol. 63, no. 3, pp. 765–771, 2010.

[73] Z. Wang, G. K. Aguirre, H. Rao, J. Wang, M. A. Fernández-Seara, A. R. Childress, and J. A. Detre, "Empirical optimization of ASL data analysis using an ASL data processing toolbox: ASLtbx," *Magnetic Resonance Imaging*, vol. 26, no. 2, pp. 261–269, 2008.

[74] Siemens AG, "Diffusion Imaging Perfusion Imaging," 2009. [Online]. Available: http://www.healthcare.siemens.com/siemens_hwemhwem_ssxa_ websites-context-root/wcm/idc/siemens_hwem-hwem_ssxa_websites-context-root/wcm/idc/groups/public/@global/@imaging/@mri/documents/download/mdaw/mty3/~edisp/diffusion_perfusion_imaging_verio_b17_eng-00032833.pdf. [Accessed: 03-Jan-2015].

[75] J. A. Wells, B. Siow, M. F. Lythgoe, and D. L. Thomas, "The importance of RF bandwidth for effective tagging in pulsed arterial spin labeling MRI at 9.4 T," *NMR in Biomedicine*, vol. 25, no. 10, pp. 1139–1143, 2012.

[76] "RF Coils," 2006. [Online]. Available: http://ric.uthscsa.edu/personalpages/ lancaster/DI2_Projects_2006/RF_Coils.pdf. [Accessed: 14-Jan-2015].

[77] H. Jahanian, "Functional MRI using pseudo-continuous arterial spin labeling," The University of Michigan, 2012.

[78] K. Restom, Y. Behzadi, and T. T. Liu, "Physiological noise reduction for arterial spin labeling functional MRI," *Neuroimage*, vol. 31, no. 3, pp. 1104 – 1115, 2006.

[79] E. B. Welch, "Motion Correction Techniques for Magnetic Resonance Imaging," Faculty of the Mayo Graduate School, 2003.

[80] "Cognitive neuroscience oh Thought Laboratory." [Online]. Available: http://www.christofflab.ca/resources/fMRI-data-analysis/preprocessing/realign/. [Accessed: 17-Jan-2015].

[81] O. Bieri and K. Scheffler, "Flow compensation in balanced SSFP sequences," *Magnetic Resonance in Medicine*, vol. 54, no. 4, pp. 901–907, 2005.

[82] Y. Jung, E. C. Wong, and T. T. Liu, "Multiphase pseudocontinuous arterial spin labeling (MP-PCASL) for robust quantification of cerebral blood flow," *Magnetic Resonance in Medicine*, vol. 64, no. 3, pp. 799–810, 2010.

Annexes

Annex A – Performance comparison of Siemens and SPM protocols for motion correction.

In this annex, the results of a separate experiment are presented. One subject was scanned with the pCASL sequence prior to the optimization tests. Perfusion was measured twice, in the first run we told the subject to avoid head movement, as usual. However in the second run, we specifically asked the subject to move his head during measurements (see **Figure A.1**). The movement was evident and could be perceived while watching the 113 images acquired. The post-processing steps included motion correction (skipped with Siemens dataset), co-registration and segmentation.

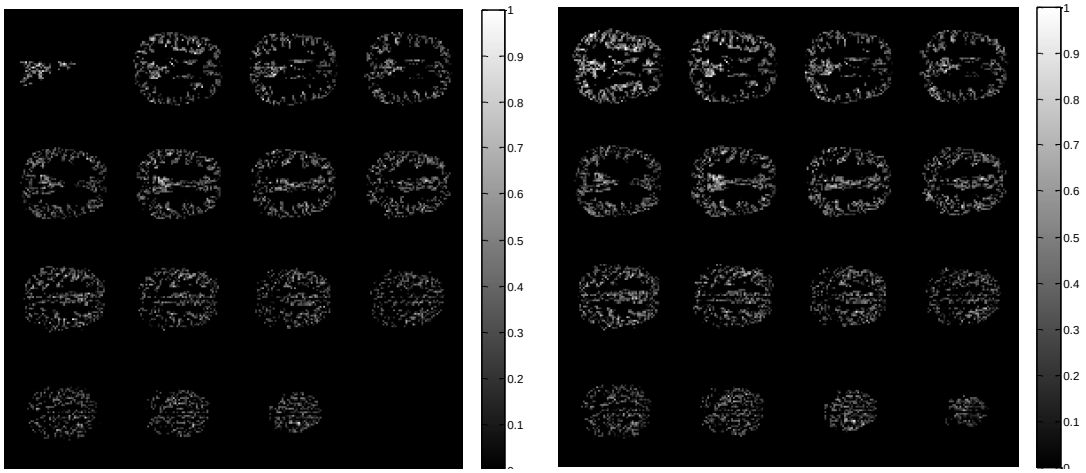

Figure A.1 – tSNR images for SPM motion correction **(left)** and for Siemens motion correction **(right)**.

Table A.1 – Average gray matter tSNR values obtained in the different protocols.

Protocols	tSNR	SD
SPM motion correction	0.20	0.02
Siemens motion correction	0.23	0.03

Annex B – Background suppression using EPI readout is not completely efficient for multislice acquisitions.

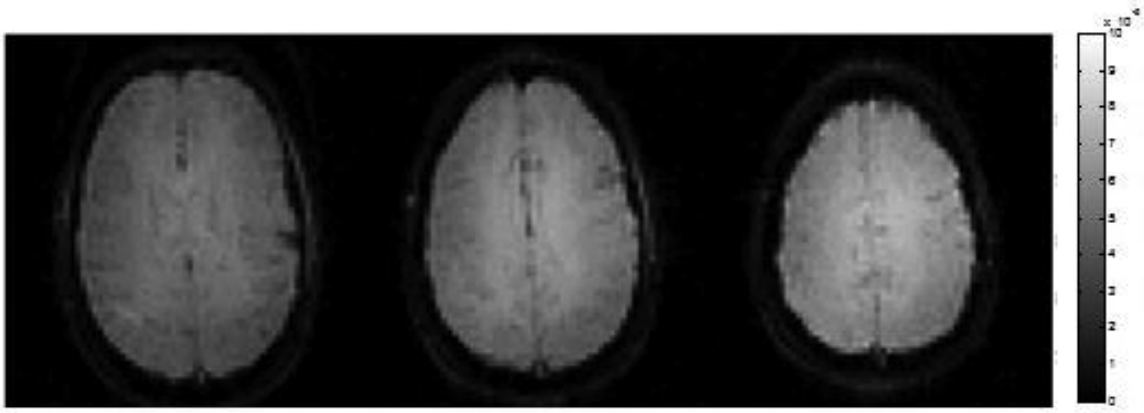

Figure B.1 – Representation of the first, fifth and eighth slices acquired with background suppression for d=0. From slice to slice a slight increase in signal is perceptible.

Annex C – Abstract submitted to the ISMRM 23rd Annual Meeting 2015

Target audience: Neuroradiologists, neurologists, neuroscientists interested in brain perfusion, pulse sequences developers.

Purpose: Pseudo continuous arterial spin labeling (pCASL)[1] is recommended as the first choice for arterial spin labeling (ASL) studies since it combines both advantages of continuous and pulsed methods, namely a high signal-to-noise ratio (SNR) and inversion efficiency[2]. SNR is typically used as a quantitative measure of image quality and provides a direct means for comparison of signal obtained with different imaging methods. In this study, we have investigated changes in four sequence parameters on the SNR of a pCASL experiment, namely the shape and flip angle of the inversion pulses, the effect of full and incomplete background suppression[3], the differences between balanced and unbalanced pCASL[4] and, finally, the readout sequence (EPI or TrueFISP[5]).

Methods: All experimental measurements were performed on a Siemens Magnetom Prisma (Siemens Medical Solutions, Erlangen, Germany) with a magnetic field strength of 3T using a 20 channel head coil. Three separated studies were performed. Initially, the balanced pCASL sequence with EPI readout was tested for 3 inversion pulse shapes with different bandwidths and 3 flip angles (20, 24, 28) for a total of 9 runs in 6 subjects. For the second study, background suppression, achieved with one saturation and two inversion pulses, was tested in 5 subjects. Since perfect background suppression causes complications in postprocessing and prohibits motion correction, the background suppression efficiency was reduced by shifting the maximum suppression in five steps from 0ms to 500ms forward. In the last study, three SNR differences between balanced and unbalanced pCASL with EPI readout and balanced pCASL with TrueFISP readout were compared.

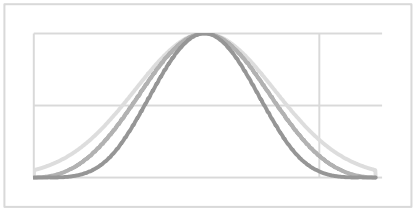

Figure1. Pulse shapes used for PCASL inversion (Gauss, F768, FDA)

Acquisition parameters for the first study: single-shot gradient-echo EPI, field-of-view (FOV)=240×240, matrix=64×64, voxel size=3×3mm, bandwidth=2.7kHz, 12 slices acquired in ascending order, slice thickness=3mm, distance factor between slices=20, labeling duration=1500ms, post spin labeling delay=1800ms, TR=4000ms, TE=21ms, number of controls/labels=54 pairs, RF duration=0.6ms, pause between RF pulses = 0.6ms, and scan duration 8.37min. For the other studies, the number of slices was reduced to eight and the optimal flip angle and pulse shape discovered previously were used. Additionally, for pCASL-TrueFISP the bandwidth and post-labeling delay were reduced to 0.98kHz and 1300ms respectively and the flip angle was set to 60º.

All background suppressed image data were saved as complex raw data and reconstructed offline with custom-made software. Data analysis was performed with homemade MATLAB software and SPM8 (Wellcome Department of Imaging Neuroscience, London, UK). Perfusion images were obtained by pairwise subtraction of control and label images and then averaged across the temporal series. Temporal SNR (tSNR) was determined as mean divided by standard deviation of the single perfusion images, averaged over the entire gray matter.

Results/Discussion:

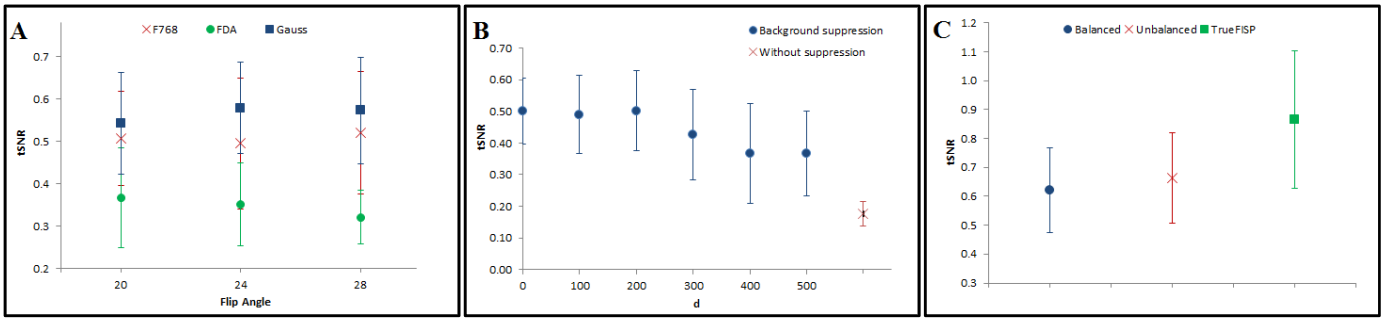

Figure2. *Mean gray matter SNR values for different inversion pulses shapes and flip angle (A), values of d (maximum suppression shift) and unsuppressed data (B), and different readouts/labeling gradient moment.*

The highest SNR obtained was 0.529 ± 0.107 for an inversion pulse with Gaussian shape and flip angle equal to 24º (Figure 2A). However, this result was closely followed by the one obtained for the same pulse but with 28º. The flip angle dependence is in accordance with previous studies[5,6]. In addition, the inversion efficiency seems to decrease with increasing pulse bandwidth. As expected, data measured with background suppression yielded a significantly higher SNR. Moving the time of optimal suppression by up to 200ms for postprocessing simplicity and motion correction is possible without significant loss in SNR (Figure 2B).
Using unbalanced pCASL did not yield a significant gain in SNR compared to the balanced sequence (Figure 2C), even though it provided in average a slightly higher SNR. TrueFISP's SNR was also not significantly different from the EPI but it showed a tendency to be higher. Its longer duration, however, limits the number of slices possible in a given repetition time.

Conclusion: Based on the results, we recommend the use of a Gaussian inversion pulse with a flip angle equal to 24º or 28º and background suppression to maximize the SNR of the resulting images.

References: 1. Garcia et al, Proceedings of ISMRM 2005, Miami, p. 37; 2. Alsop et al, MRM 2014; 3. Ye et al, MRM 2000, 44:92-100; 4. Wu et al, MRM 2007, 58:1020-1027; 5. Park et al, MRI 2013, 31:1044-1050; 6. Pohmann et al, MRM 2010, 63:438–46.